Faculty of Applied Sciences

Department of Physics

Ph.D. Thesis

Reactive magnetron sputtering of thin films with unique properties

Sergei Zenkin

Submitted to acquire the degree of Doctor of Philosophy in the field of Plasma Physics and Physics of Thin Films

Supervisor: Prof. Ing. Jindřich Musil, DrSc.

Date of submission:

Pilsen 2017

Fakulta aplikovaných věd

Katedra fyziky

Disertační práce

Reaktivní magnetronové naprašování tenkých vrstev s unikálními vlastnostmi

Sergei Zenkin

K získání akademického titulu doktor v oboru Fyzika plazmatu a tenkých vrstev

Školitel: Prof. Ing. Jindřich Musil, DrSc.

Datum odevzdání:

Plzeň 2017

Declaration

I hereby declare that I wrote this submitted thesis myself by using the results obtained and published during my Ph.D. study and by using properly cited literature.

The thesis includes the results obtained during my Ph.D. study at the Department of Physics and NTIS, European Centre of Excellence, University of West Bohemia, since January 2013. This research was financially supported by the projects SGS–2013–045 (2013–2015): New thin-film materials and plasma deposition systems, and SGS–2016–056 (2016-2018): New nanostructured thin-film materials formed by plasma technologies.

Pilsen, 2017   ……………………………………………

Acknowledgments

Contents

1. General introduction

2. Aims of this thesis

3. Hydrophobicity of thin films of compounds of low-electronegativity metals

4. Flexible hydrophobic ZrN films

5. Thickness dependence of wetting properties and surface free energy of HfO$_2$ thin films

6. Physical and mechanical properties of crystalline and nanocrystalline Zr-Ti alloy prepared by DC magnetron sputtering

The thesis is submitted in a form of four scientific papers published (Ch3.-Ch.5) or submitted for publication (Ch.6) in prestigious international journals. These papers include the most important results obtained during my Ph.D. study at the Faculty of Applied Science, University of West Bohemia in Pilsen since January 2013.

I carried out all depositions of the low-electronegativity-metal oxides and nitrides (Ch.3), zirconium nitride films (Ch.4) and ZrTi(O) films (Ch.6) together with the corresponding measurements of the film thickness, morphology, mechanical and hydrophobic properties of these films. I am the author of the main idea and I have done the hydrophobicity and free surface energy measurements (Ch.4). Also, I participated in interpretation of the results obtained for the elemental composition, phase composition, SEM morphology, and Raman measurement of the films by my colleagues (Ch3.-Ch.6).

CHAPTER 1

_____

GENERAL INTRODUCTION

_____

1.1 Thin film processing

1.1.1 Principles of plasma discharges

Plasma is usually called the fourth state of matter in addition to solid, liquid and gas. It is an assembly of ionized atoms and molecules, charged ions and electrons. Plasma is an electrically neutral medium, which means that the density of positively charged ions is equal to the density of negatively charged ions and electrons. The change from the gas state to the plasma state occurs when the temperature of atoms is sufficiently high and they decompose into charged particles. The easiest way to achieve this is a plasma discharge. Normally, a low-pressure plasma discharge is a strongly non-equilibrium process where the applied power heats the electrons due to their lower mass in comparison with the mass of ions. These heated electrons have high enough kinetic energy and high possibility to ionize atoms during collisions. The ratio between charged and neutral particles in the plasma discharge is called the degree of ionization and is very important in the case of plasma deposition process [1].
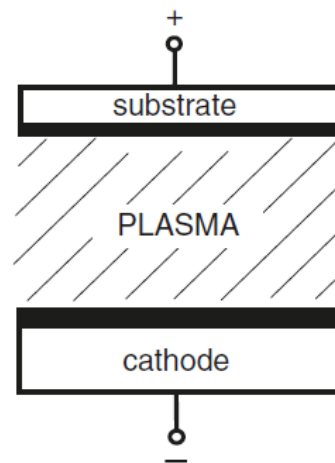
Fig.1.1 Scheme of a simple DC electrical discharge [2]

Fig. 1.1 shows a simple electrical discharge. It consists of two electrodes and a power source. Upon application of a dc voltage between the electrodes a discharge is formed after the breakdown of the working gas. Electrons emitted from the cathode are accelerated to the anode and generate positively charged ions by collisions with heavy particles. These heavy ions flow to the cathode and collide with its surface with sputtering of cathode material [3]. Also, these collisions are the source of secondary electrons. These secondary electrons play an important role in the gas ionization mechanism, described by John Townsend. His equation shows his criteria of the transition from a nonstationary to a self-sustaining discharge:

$$\gamma e^{\alpha d} = 1$$

here:

γ – Townsend coefficient of secondary emission

α – Townsend coefficient of ionization

d – A distance between cathode and anode

According to this formula, a self-sustaining discharge arises when each emitted electron creates 1 secondary electron which takes over its function.
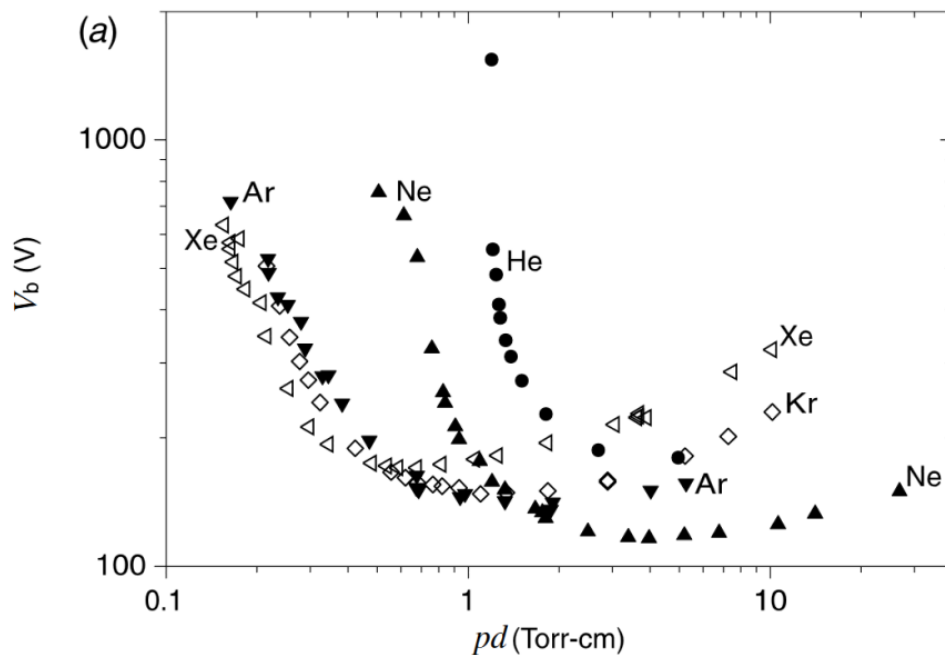
Fig.1.2 Paschen curves for noble gases [1]

Both coefficients α and γ are strongly dependent on the working pressure and distance between the electrodes. This dependence was experimentally determined by Friedrich Paschen, who obtained the breaking voltage as a function of the gas pressure, distance between two electrodes and the type of gas. Fig.1.2 shows typical Paschen curves for noble gases.

The current-voltage characteristic of a dc discharge can be divided onto several regimes, which are characterized by a completely different degree of ionization and energies of electrons and ions. Typical I-V characteristic is shown in Fig.1.3. Three characteristic regimes can be determined:

1) Townsend discharge or dark discharge where the current increases with only little increase of the voltage and the free electrons carry enough energy for further ionization.
2) Glow discharge. In this regime the voltage drops and the current increases to the milliampere range. At low current, the voltage is current-independent. At higher current, the normal glow turns into the abnormal glow and the voltage gradually increases.
3) Arc discharge. In this regime the current achieves the ampere range and the voltage significantly drops with increasing of current.
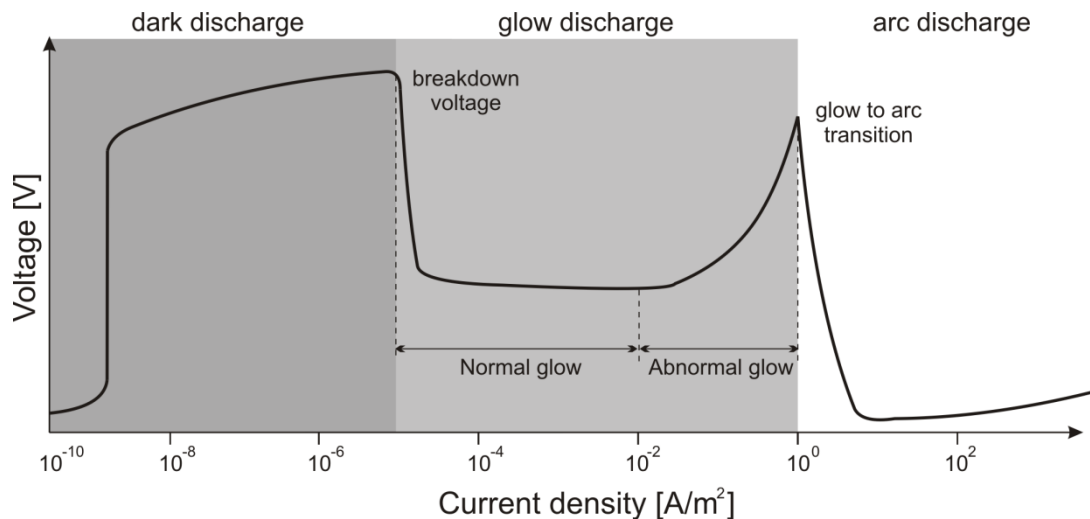
Fig.1.3 Volt-ampere characteristics of the dc discharge

1.1.2 Physical sputtering

The physical sputtering is a process whereby particles are ejected from a solid target material due to bombardment of the target by energetic particles [1]. These energetic particles, usually ions of noble gas, are accelerated by electrical field and transfer the momentum to the atoms of target material by collisions [1-3].

Sputter deposition of thin films as a term then characterizes the process where a surface being sputtered serves as the source of the deposited material. The sputtered particles are transported from the target to the substrate typically without collisions in a plasma discharge [1]. Probability to sputter an atom from the surface of the target depends on the energy of the incident particle and its mass.

Another important parameter is the sputtering yield which is the ratio of sputtered particles to bombarded particles and characterizes the sputtering efficiency. Sputtering yield depends on a number of parameters such as the nature and strength of bonds in the target material, target elemental composition and the angle of flux of bombarded particles. It is relatively insensitive to the target temperature [4].

Sputtering yields of elements or compounds are determined experimentally. It is characterized by the erosion rate, which is determined as:

$$R = \frac{\gamma \times J}{n \times e} \text{ (cm/min)}$$

where J is the ion current density in mA/cm^2, γ is the sputtering yield in atoms/ion, e is the elemental charge, and n is the density of the target material in g/cm^3 [1].

1.1.3 Magnetron discharge
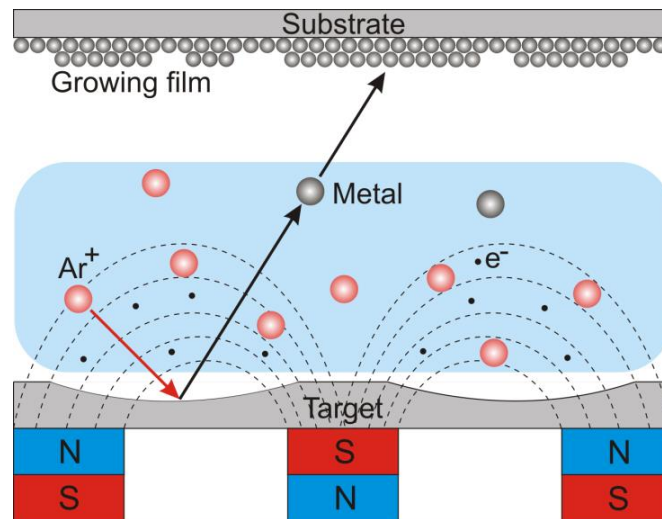
Fig.1.4 Scheme of magnetron sputtering

Magnetron sputtering is a widely used technique for thin film deposition. A simplified scheme of the magnetron is given in Fig.1.4. It is an abnormal glow discharge in the crossed electric and magnetic fields. Electrons emitted from the target due to argon bombardment are held in the magnetic "trap" near the target and ionize neutral argon atoms due to collisions [2, 3]. Charged ions of the working gas accelerate to the target and eject atoms of the sputtered material, for example metal, by momentum transfer. Metal atoms flow through the magnetic field and settle on the substrate which is located in front of the target. A high concentration of electrons near the target results in a high probability of ionization of the working gas, usually Ar [1]. A high ionization of the plasma allows to operate at low pressures and high discharge currents resulting in a significant deposition rate of the film [5, 6]. Also, due to advantages of magnetron sputtering such as preparation of high quality defect-free films [6], high deposition rate [5, 6], easy control of elemental composition and structure of the growing film [7], it is widely used in various industrial applications such as optical coatings [8], hard coatings for cutting tools [9-12], decorative coatings [13], microelectronics [14], solar cells [15] and so on.

It is important to note that magnetron sputtering can in addition be easily modified, for example by [2, 3]:

1) Increasing the degree of ionization (hollow cathode, additional RF source)

2) Modification of the voltage waveform (DC, AC, RF, DC pulsed, HiPIMS)

3) Introduction of the reactive gas into the discharge

4) Modification of the magnetic field (conventional or unbalanced magnetron, mirror or closed magnetic field configuration of dual magnetron)

5) Co-sputtering with other deposition techniques like ECR or CVD

1.1.4 Reactive sputtering

Magnetron sputtering can be divided onto non-reactive and reactive sputtering. In the first case, the films produced by sputtering of an elemental target in a noble gas atmosphere. The second way is to introduce a certain amount of the reactive gas, such as oxygen or nitrogen, in addition to the working gas. Reactive sputtering is a fine-tuned and flexible process which allows to produce oxides, nitrides, carbides, oxynitrides and other materials. In the case of non-conducting materials, for example AlN, it is possible to produce it from a pure metal Al target without using a complex RF sputtering. Unfortunately, the deposition rate in the reactive sputtering is lower than the rate for a pure metal deposition due to the several reasons [2, 16]:

1) Sputtering yield for a compound is lower than the corresponding for metal $\gamma_{Me} > \gamma_{com}$, e.g. $\gamma_{Ti} > \gamma_{TiN}$

2) Reactive gases typically have low atomic mass; therefoer they are highly ineffective in sputtering.

3) Decrease of the magnetron discharge voltage due to replacing of pure metal by its compound, for example Ti replaced by TiN.

This reduction follows from the phenomenon called the target poisoning. Chemical reactions and formation of the compound occurs on the surfaces of the substrate and the target [2].
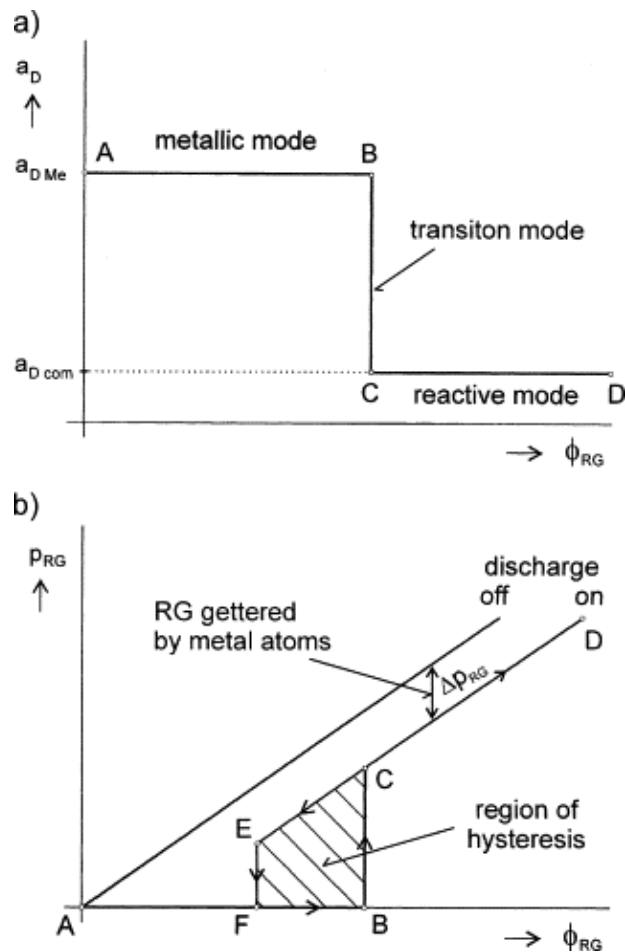

Fig.1.5 Hysteresis effect [16]

The reactive magnetron sputtering can be divided onthe metallic, transition and reactive regime in dependence on the amount of the reactive gas in the sputtering atmosphere [2], Fig.1.5a. During the preparation of non-stoichiometric films the key problem is the hysteresis effect. It can be divided onto the 2 processes [16]:

1) The sputtering of the target surface and

2) The covering of its surface by reaction products.

Fig. 1.5b illustrates the dependence of the reactive gas partial pressure, p_{RG}, as a function of the flow rate, ϕ_{RG}, of the reactive gas supplied into the deposition chamber with and without the discharge. The hysteresis occurs in the presence of the discharge only [2]. At low values of the reactive gas flow rate all reactive gas is gettered by the sputtered metal. At point B, the flow rate into the chamber is equal to the gettering rate of sputtered metal. After crossing this point, a small increase of the sputtering gas leads to:

1) Increase of the partial pressure of the reactive gas
2) Decrease of the deposition rate

A further increase of ϕ_{RG} results in a linear increase of p_{RG} and almost constant a_D, which is typical for the reactive mode of sputtering. The decrease of ϕ_{RG} from D to E is accompanied by a decrease of p_{RG}, but a return to the metallic mode (interval EC) is delayed [16]. This effect occurs due to the fact that p_{RG} stays high until the compound layer of the sputtered material is removed. As a result, the consumption of the reactive gas increases and p_{RG} decreases to the background level. A closed hysteresis loop is formed in this way.

In order to reduce the hysteresis several methods can be used [2, 16]:

1) Using of sputtering systems with a pumping speed larger than a critical pumping speed.
2) Using of sputtering systems controlled by plasma emission monitoring.
3) Gas pulsing
4) Using of dual magnetrons, magnetrons with a full target erosion or magnetrons equipped with substoichiometric ceramic targets.

1.2. Film growth

1.2.1 Nucleation and growth

The process of the film formation starts when the clean substrate material is exposed to a flux of the sputtered atoms. Atoms which came to the surface form chemical bonds with atoms of the substrate. Also, the mobility of the sputtered atoms on the surface is relatively high, therefore they are settling down on the equilibrium positions. [4]

Several models have been suggested for the description of the film growth:

1) Frank–van der Merve growth mode or layer by layer growth mechanism.

The layer-by-layer growth mechanism of Frank-van der Merwe happens when film atoms bind more to the substrate than with each other. The growth of the next layer does not begin until the

complete formation of the previous one is finished, so there is a distinctly two-dimensional growth, Fig.1.6.a.

2) Vollmer – Weber growth mode or mechanism of island growth.

Mechanism of island growth happens when atoms in the film bind more with each other than with the substrate surface. In this case three-dimensional islands are created and grow directly on the substrate surface, Fig.1.6.b.

3) Stranski-Krastanov growth mode.

This mode is a combination of the previous two. It describes the case when the growth starts as two-dimensional (layered) and then change to a three-dimensional (island). After completion of the two-dimensional layer growth the three-dimensional island growth occurs. The nature and thickness of the two-dimensional layer (often referred to as a Stranski – Krystanov layer) depends on the individual case, Fig.1.6.c.
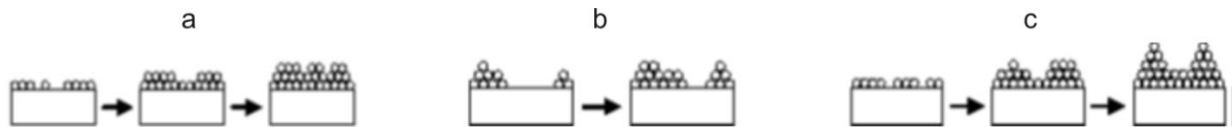
Fig. 1.6 Basic modes of thin film growth: a) Frank-van der Merwe, b) Volmer-Weber and c) Stranski-Krastanov [17]

1.2.2 Structure zone models and microstructure

After the formation of several angstroms of the sputtered material on the substrate surface macro and microstrucrure of the growing film will strongly depend on the sputtering conditions such as the substrate temperature or the energy of the neutral and charged particle bombardment. Several structure-zone models have been reported in order to predict the microstructure and morphology of the sputtered films in dependence on the deposition parameters.
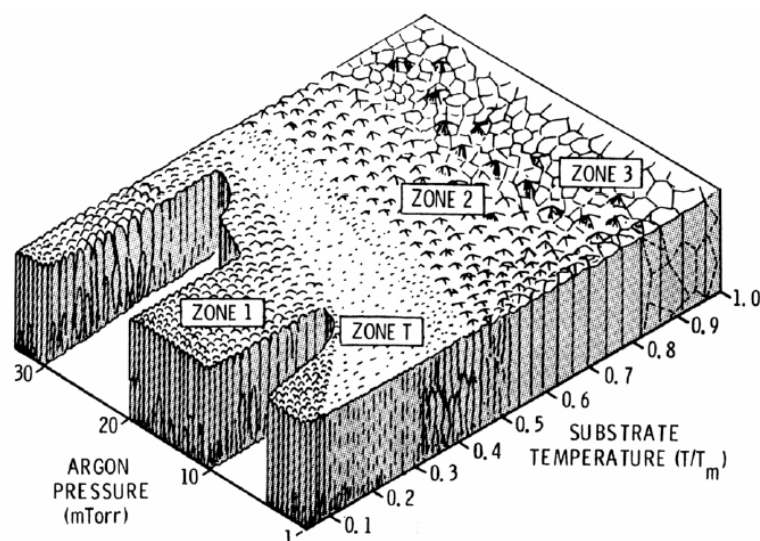
Fig.1.6 Thornton's structure-zone diagram [18]

The most used structure-zone diagram was suggested by Thornton [18], Fig.1.6. It shows the dependence of the microstructure of the growing film on the of total pressure and substrate temperature normalized to the melting point of the sputtered material.

Four characteristic zones can be determined in this diagram:

1) Zone 1 ($T_s/T_m < 0.2$-0.3, where T_s is the substrate temperature and T_m the melting point of the material). This zone is characterized by the fine-textured fibrous grains due to the very low mobility of sputtered atoms on the substrate surface. Also, the porous structure typically shows very high values of the surface area, which is important for some applications. This structure is thermally unstable, with high recrystallization during the heating to temperatures higher than the deposition temperature.

2) Zone 2 ($0.3 \leq T_s/T_m < 0.5$). This zone is characterized by the densification of the film and growth of the grain sizes. Typically, the grain width is not higher than film thickness and strongly depends on the deposition temperature.

3) Zone 3 ($T_s/T_m \geq 0.5$). In this zone high recrystallization occurs, which is characterized by high, well defined crystals of sputtered material. The thin film can switch from columnar structure to highly crystalline, where the width of the crystals is higher than film thickness.

4) Zone T. A transition zone between zones 1 and 2 characterized by a densified crystalline structure with small grains achieved by bombardment of the surface by high energy neutral particles at low total pressure.

This simple model allows to predict the microstructure of the deposited films in dependence on two deposition parameters. An extended structure zone diagram, suggested by Anders, includes energetic deposition, characterized by a large flux of ions typical for deposition by filtered cathodic arcs and high power impulse magnetron sputtering [19].
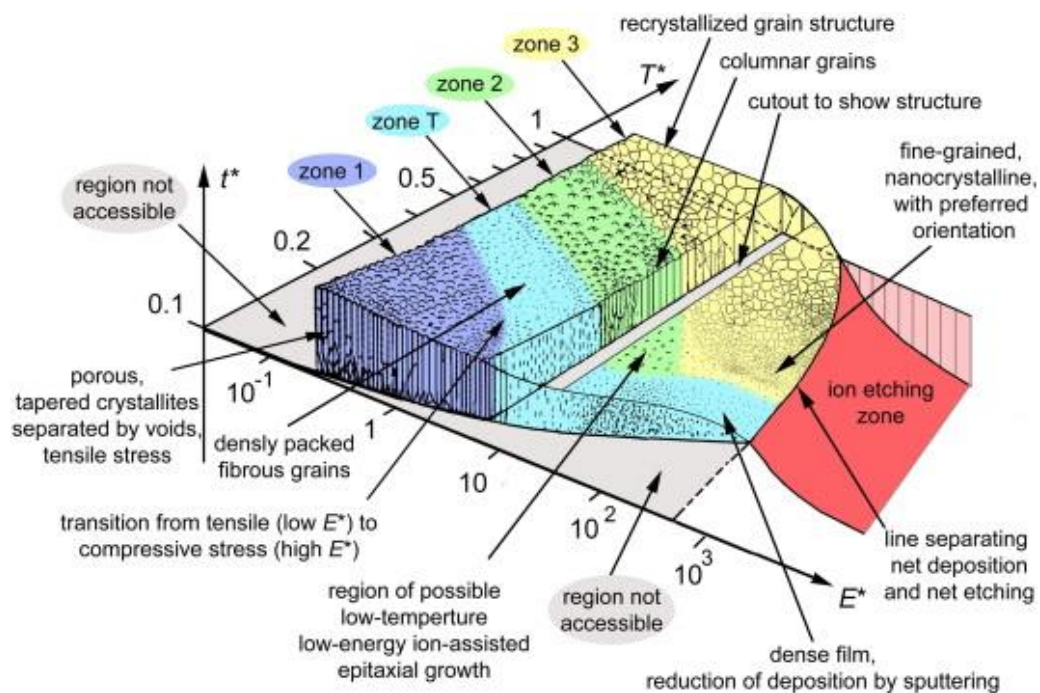

Fig.1.7 Structure zone diagram applicable to energetic deposition [19]

It shows the dependence of the film microstructure on the generalized temperature, which is the temperature of the substrate plus a temperature shift caused by the potential energy of particles arriving on the surface [19], and normalized kinetic energy of bombarding particles.

A generalized temperature is defined here as:

$$T^*=T_h+T_{pot}$$

where T_h is the ratio of the substrate temperature to the melting point of the material and T_{pot} is the characteristic temperature of a heated region affecting the rearrangement of N_{moved} atoms:

$$T_{pot} = E_{pot}/(kN_{moved})$$

The normalized kinetic energy is defined as:

$$E_{kin} = E_0 + QeV_{sheath}$$

where Q is the ion charge state number, e is the elementary charge, and V_{sheath} is the voltage drop between the plasma and the substrate surface.

This model is three-dimensional, therefore it can show the reduction of the film thickness during the intensive bombardment, or show the zone of ion etching with "negative thickness" [19], Fig. 1.7. This model in addition to the 4 zones of Thornton's diagram predicts other structures of growing films such as the fine-grained nanocrystalline structure or a possible zone of low-energy epitaxial growth.

1.3 Characterization of thin films

1.3.1 Stress measurement

Stress is a physical quantity that expresses the internal forces that neighboring particles of a continuous material exert on each other. The control of the stress in a growing film is very important, since high values of either tensile or compressive stress, especially in combination with poor adhesion, can lead to cracking or delamination of the film from the substrate [4]. The total stress in the film can be divided onto the thermal stress due to the mismatch of thermal expansion coefficients of the substrate and the growing film and the intrinsic stress of the growing film due to the phase transformation, chemical reactions, recrystallization and concentration of defects during the film growth. The residual stresses cause also a lattice strain. It represents a stored energy in the lattice that plays an important role in the resistance of the film to plastic deformation [4]. Tensile residual stress bends the substrate concavely upward, while compressive stress bends the substrate concavely down, Fig. 4.1. The deflection of the coated substrate before and after deposition is the commonly used technique for the measurement of the film stress. If the ratio of the film thickness to the substrate thickness is very low, by knowing the mechanical properties of the substrate and film material, the film thickness, and the substrate deflection, the film stress can be calculated via the modified Stoney formula [21]:

$$\sigma_f = \frac{E_s}{1-v_s} \frac{h_s^2}{6h_f R}$$

where σ_f is the average stress on the plane of the film, $\boldsymbol{E_s}$ is the biaxial elastic modulus of the substrate, ν_s is the Poisson's ratio of the substrate, h_s is the substrate thickness, h_f is the film thickness, and $1/R$ is the system curvature.
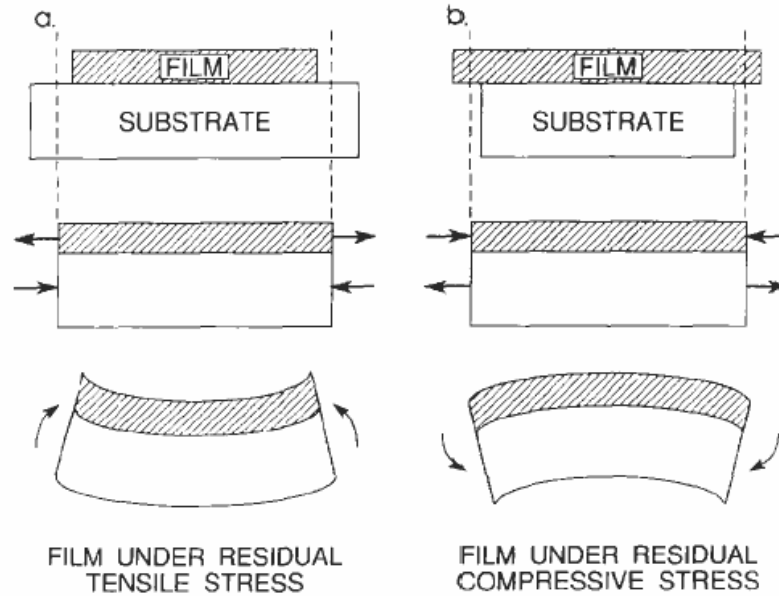
Fig. 1.8 Illustration of tensile (a) and compressive (b) stress in the film [20]

If the coating was prepared at elevated temperatures and the thermal expansion coefficients of the substrate and the film are known, the thermal stress can be calculated as:

$$\sigma_{th} = \frac{E_S}{1-\nu_S} \Delta\alpha\Delta T$$

where σ_{th} is the thermal stress of the film, $\Delta\alpha$ is the difference in thermal expansion coefficients of the film and the substrate, ΔT is the difference of the temperature before and after the deposition, $\boldsymbol{E_s}$ is the biaxial elastic modulus of the substrate, and ν_s is the Poisson's ratio of the substrate.

1.3.2 Hardness and Youngs modulus

Hardness is a measure of how resistant a solid is to various shape changes when a compressive force is applied [22]. In other words, it is the resistance of a material to plastic deformation. Various measurement techniques are used for the determination of hardness on the macro and micro scale. Most of them are based on the measurement of the penetration resistance of the material to a permanent deformation by a special indenter. The two most commonly used microhardness tests in the case of thin-film measurements are:

1) Vickers hardness test (HV)

2) Knoop hardness test (HK)

During the test an indenter with known geometry is pressed into the material with a constant load and the depth of penetration is used for calculation of the hardness of tested material. A typical load-displacement curve is shown on Fig.1.9.

In order to remove the elastic contribution to the displacement and determine the projected area from the load-displacement curve the Oliver and Pharr model can be used [23]:

$$S = \frac{dP}{dH} = \frac{2}{\sqrt{\pi}} E_r \sqrt{A}$$

Where $S = dP/dh$ is the experimentally measured stiffness of the upper portion of the unloading data, E_r is the reduced modulus, and A is the projected area of the elastic contact.
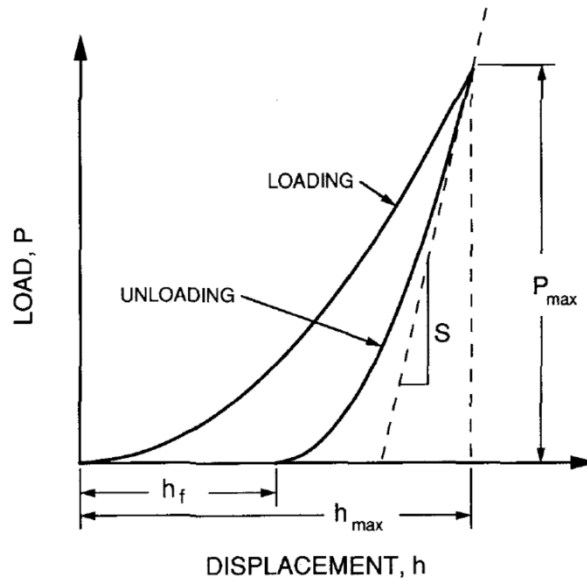
Fig. 1.9 Schematic representation of the load versus indenter displacement data for an indentation experiment. The quantities shown are P_{max} - the peak indentation load; h_{max} - the indenter displacement at peak load; h_f - the final depth of the contact impression after unloading; and S - the initial unloading stiffness [23]

The reduced modulus is defined as:

$$\frac{1}{E_r} = \frac{1 - v^2}{E} + \frac{1 - v_i{}^2}{E_i}$$

Here, E and v are the Young's modulus and the Poisson's ratio of the film respectively, and E_i and v_i are the same parameters for the indenter.

1.3.3 Resistance to cracking

One of the important mechanical parameters of the hard thin films is their toughness and resistance to cracking [24]. Two most common methods for the determination of the film resistance to cracking are: high indentation load test and bending test. In the high indentation load test a diamond indenter penetrates into the surface of the film with a high indentation load L>250mN increasing up to its cracking. During the bending test films deposited on the flexible

substrate, typically molybdenum foil, are bent around the cylinder with a fixed diameter. The resulting strain in the film can be calculated as [25]:

$$\varepsilon_{cr} = \frac{(l_f - l_0)}{l_0} = \frac{\alpha(r_f - r_0)}{\alpha r_0} = \frac{(h_s + h_f) + 1}{2r_c}$$

The lengths l_f and l_0 and radii r_f, r_0 and r_c are defined in Fig.1.10. From this formula it is clearly seen that the strain ε induced in the bent film can be increased by decreasing the radius r_c around which the coated metallic strip is bent [25].
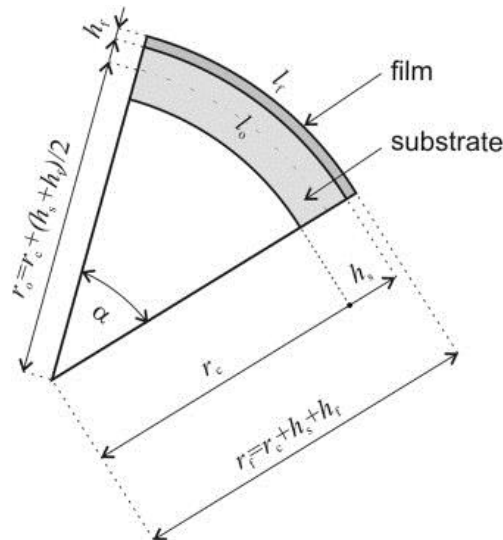
Fig. 1.10 Geometry of the bent substrate covered by the film. The coated substrate is bent around the cylinder of radius r_c [25]

After the test cracks can be detected by the optical or electron microscopy. Typical images are given in Fig.1.11
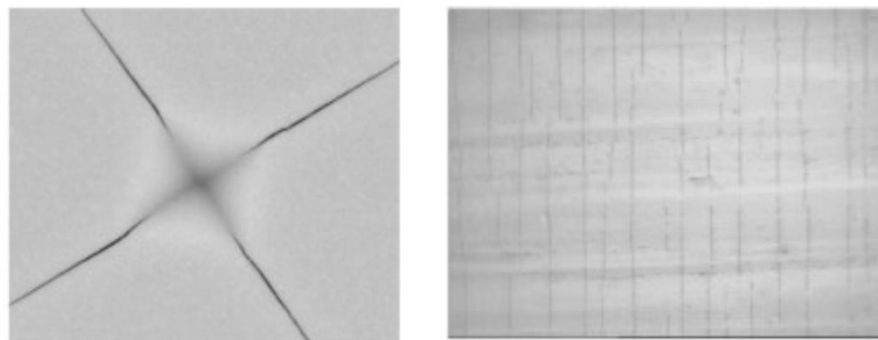
Fig. 1.11 Cracks formation after a) high indentation load test and b) bending test [25]

1.3.4 Contact angle

The contact angle is the angle, measured through the liquid, at which a liquid–vapor interface meets a solid surface [26]. The contact angle quantifies the wettability of the solid by the liquid, therefore for a given solid and liquid at a given pressure and temperature the contact angle has a unique value [26]. In the case of wetting by water all surfaces can be divided onto hydrophilic (or wetted) with water contact angle lower than 90º and hydrophobic (or nonwetted) with water

contact angle higher than 90º. Wettability in the system vapor-liquid-solid is determined by the Young's equation:

$$\gamma_{SV} = \gamma_{LV} \times cos\theta + \gamma_{SL}$$

where γ_{LV} is the liquid surface tension, γ_{SV} is the solid surface tension, γ_{SL} is the solid–liquid interfacial tension, and θ is the contact angle. Equilibrium between these forces gives the static contact angle of the system, Fig.1.12.
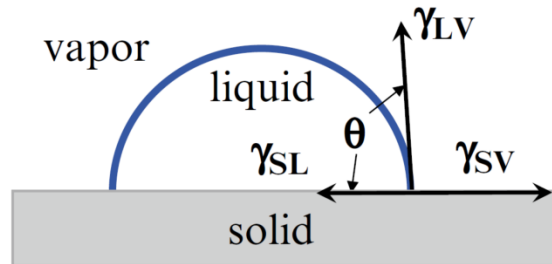
Fig. 1.12 Contact angle and surface tensions in the system vapor-liquid-solid [26]

Common surfaces such as metals, glasses or ceramics due to their strong chemical bonds (metallic, ionic or covalent) usually show very high values of surface energy and are completely wetted by water. In comparison, surfaces of polymers with low-energy forces (for ex. van der Waals forces) show very low surface energy and therefore are not wetted by water.

It is important to note that roughness of the solid plays an important role in the surface wettability. This influence was described by Robert N. Wenzel using a simple formula:

$$cos\theta^* = R \times cos\theta$$

where θ^* is the measured contact angle, R is the roughness ratio of true area of the solid surface to the apparent area and θ is the measured contact angle for a smooth surface.

The roughness ratio R increases the contact angle for hydrophobic surfaces and decreases its value for hydrophilic surfaces, so a rough hydrophobic material becomes more hydrophobic while a hydrophilic one becomes more hydrophilic. This equation shows the importance of control of the material roughness for comparison of the wettability of different materials.

1.3.5 Gibbs free surface energy

While the free surface energy characterizes the wetting properties of the material, is is important to know how it correlates with the contact angle.

Various models are used for characterization of the surface energy, for example:

1) Zisman model
2) Fowkes model
3) Wu model
4) Owens–Wendt–Rabel–Kaelble (OWRK) model
5) van Oss, Chaudhury, and Good (vOCG) model

These models can be divided onto one-component (Zisman), two-component (Fowkes, Wu and OWRK) and three-component (vOCG) theories depending on the number of the measured surface energy components. The most useful vOCG theory allows to determine not only the total surface energy of the solid, but also its polar and non-polar components.

The van Oss-Chaudhury-Good equation can be written as:

$$\gamma_L(1+\cos\theta) = 2\left(\sqrt{\gamma_S^{LW}\gamma_L^{LW}} + \sqrt{\gamma_S^+\gamma_L^-} + \sqrt{\gamma_S^-\gamma_L^+}\right)$$

where γ_L is the surface tension of the testing liquid, θ is the measured contact angle, $\gamma_S^{LW}, \gamma_L^{LW}$ are the Lifshitz - van der Waals components of the surface energy of the solid and the liquid, respectively, and γ_S^+, γ_L^- are the polar components of the surface energy of the solid and the liquid.

Due to the fact that the van Oss-Chaudhury-Good equation contains three unknown values, in this method three reference liquids with known components of surface energy are used, Table 1.1.

Table 1.1 Surface tension components of the testing liquids

Liquid	γ^{TOT}	γ^{LW}	γ^{AB}	γ^+	γ^-
Water	72.8	21.8	51.0	25.5	25.2
Glycerol	64.0	34.0	30	3.92	57.4
α- Bromonaphthalene	44.4	43.4	≈0	0	0

1.3.6 X-ray diffraction

XRD is a standard nondestructive analysis technique for determination of the structure and quality of thin films. It is used for phase analysis, texture, residual stress, lattice parameters or grain size measurements.

In the method, diffraction of X-ray waves on a regular array of the crystal atoms by the elastic scattering leads to producing of diffraction pattern. These X-ray diffraction patterns are determined by the Bragg's law:

$$n\lambda = 2d\times\sin\theta$$

where λ is the wavelength of the beam, n is any integer, d is the spacing between the diffracting planes and θ is the incident angle.

1.3.7 Scanning electron microscopy

The scanning electron microscope is an electron microscope which produces images of a sample by scanning it with a focused beam of electrons. The angular resolution of optical microscopes is

limited by the wavelength of the visible spectra. Replacing of photons by electrons, which have a lower wavelength, allows to achieve the resolution down to 0.4nm.

The electron beam generated by an electron gun is focused on the sample. Primalry electrons interact with the sample material and generate secondary electrons, X-ray radiation, Auger electrons and so on, which can be detected by special detectors. The intensity of these signals strongly depends on the topography of the tested material.

The main types of signals that generated and detected during the operation of SEM:
1) Secondary electrons
2) Reflected electrons
3) Electrons passed through the sample
4) Electron backscatter diffraction
5) X-ray radiation
6) Light signal in the case of cathodoluminescence

Also, recently reported environmental scanning electron microscope allows to work with "wet" uncoated samples in a gaseous environment in the specimen chamber, for example Fig. 1.13.
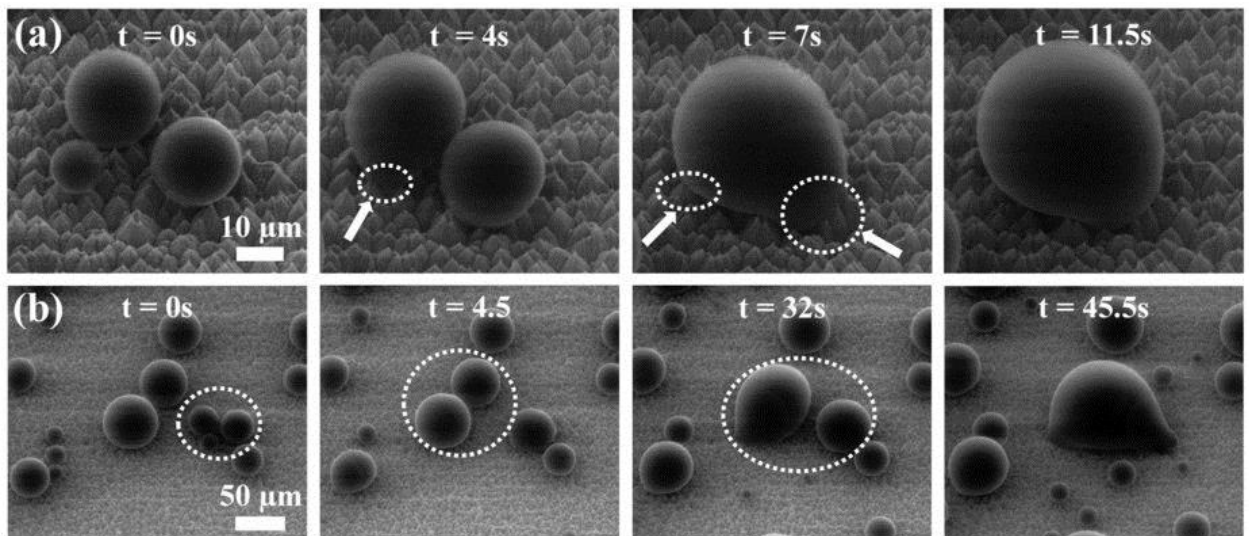
Fig. 1.13 ESEM image of the water droplet on the superhydrophobic surface [27]

1.4 References

[1] M.A. Lieberman, A.J. Lichtenberg, *Principles of plasma discharges and materials processing*, Wiley, New York, 2005.

[2] J. Musil, J. Vlcek, P. Baroch, *Magnetron Discharges for Thin Films Plasma Processing, chapter in Materials Surface Processing by Directed Energy Techniques*, Elsevier, 2006.

[3] A.I. Kuzmichev, *Magnetron sputtering systems*, Avers, 2008 (in Russian).

[4] R. Daniel, *Enhanced properties of alloyed transition metal nitride films*, PhD thesis.

[5] J.Musil, P. Baroch, Vacuum 87, 2013, 96.

[6] J. Vlček , J. Rezek, J. Houška, T. Kozák, J. Kohout, Vacuum 114, 2015, 131.

[7] Y. Zou, H. Ma, R. Spolenak, Nature communications. 6:7748, 2015.

[8] S.J. Pearce, , M.D.B. Charlton, J. Hiltunen, J. Puustinen, J. Lappalainen, J.S. Wilkinson, Surface and Coatings Technology 206, 2012, 4930.

[9] Mayrhofer, P.H., Mitterer, C., Musil, J., Surface and Coatings Technology 174–175, 2003, 725.

[10] Musil, J., Zeman, P., Hrubý, H., Mayrhofer, P.H., Surface and Coatings Technology 120–121, 1999, 179.

[11] Petrov, I., Hultman, L., Helmersson, U., Sundgren, J.-E., Greene, J.E., Thin Solid Films 169, 1989, 299.

[12] Mayrhofer, P.H., Mitterer, C., Hultman, L., Clemens, H., Progress in Materials Science 51, 2006, 1032.

[13] Furrer, A., Spolenak, R., Acta Materialia 66, 2014, 241.

[14] Mühlbacher, M. et al. Journal of Applied Physics 118, 101063.

[15] A.D. Compaan, A.Gupta, S.Lee, S.Wang, J.Drayton, Solar Energy 77, 2004, 815.

[16] Musil, J., Baroch, P., Vlček, J., Nam, K.H., Han, J.G., Thin Solid Films 475, 2005, 208.

[17] J.E. Greene, *Handbook of crystal growth*, Elsevier, 1993.

[18] J.A. Thornton, Journal of Vacuum Science & Technology 11, 1974, 666.

[19] A. Anders, Thin Solid Films 518, 2010, 4087.

[20] M. Ohring, *The material science of thin films*, Academic Press, 1992.

[21] J.D. Wilcock, D.S. Campbell, Thin Solid Films 3, 1969, 3.

[22] J. Malzbender, Journal of the European Ceramics Society 23, 2003, 1355.

[23] W.C. Oliver, G.M. Pharr, Journal of Materials Research, 1992, 1564.

[24] Musil, J., Surface and Coatings Technology 207, 2012, 50.

[25] J. Musil ,J. Blažek,K. Fajfrlík, R. Čerstvý, Surface and Coatings Technology 264, 2015, 114.

[26] K. Law, H. Zhao, *Surface Wetting Characterization, Contact Angle, and Fundamentals*, Springer, 2016.

[27] H.Jo, K.Hwang, D.Kim, M.Kiyofumi, H.Park, M.Kim, H.Ahn, Scientific Reports 5,2015, 9901.

2. AIMS OF THIS THESIS

The subject of the Ph.D. thesis is the preparation of new alloy and metal nitride films with multifunctional properties and an enhanced resistance to cracking by magnetron sputtering and the investigation of the interrelationships between the deposition parameters and the film properties.

The aims of the Ph.D. thesis are the following:

1. To demonstrate that the nitride and oxide films made of the low-electronegativity metals are hard hydrophobic ceramic films similarly as the oxide films made of the rare-earth elements. To compare the wettability of the surface of the nitride and oxide films made of the low-electronegativity metals.

2. To investigate the effect of the energy E_{bi} delivered to the growing film by bombarding ions on its mechanical properties, resistance to cracking and water droplet contact angle.

3. To investigate the structure, microstructure, physical and mechanical properties of the Zr-Ti alloy films with different elemental composition and to find the conditions under which the Zr-Ti alloy films will exhibit enhanced hardness and resistance to cracking.

CHAPTER 3

HYDROPHOBICITY OF THIN FILMS OF COMPOUNDS OF LOW-ELECTRONEGATIVITY METALS

3.1 Introduction

Hydrophobicity of materials surfaces is desirable for various applications. It is often achieved by surface modification, e.g. by attaching organic polymers [1] or, in case of superhydrophobicity, by patterning the surface [2]. Such surface modifications are, however, not suitable for harsh environment applications as polymers decompose chemically and/or thermally and surface patterns are destroyed mechanically. Here we show that oxides and nitrides of various low-electronegativity [3] metals are hydrophobic hard ceramics. We attribute their hydrophobicity to low Lewis acidity of the low-electronegativity cations implying a low ability of the cations on the surface to form coordinate bonds with water oxygen anions. Furthermore, we observe a systematically stronger hydrophobic behavior of nitrides compared with the corresponding oxides, which we attribute to nitrogen being a poorer Lewis base than oxygen due to a reduced number of lone pairs of electrons, implying a lower ability of nitrogen anions on the surface to form hydrogen bonds with water hydrogen cations. Most of the oxides and nitrides investigated exhibit high values of hardness. Therefore oxides and nitrides of low-electronegativity metals should find application as hydrophobic materials in harsh conditions.

Typically, metal-based ceramics exhibit useful functional properties, such as high hardness, toughness, and high melting point. But in their nature they tend to be hydrophilic due to a high polarity of their surfaces. In a recent paper [4], Azimi et al. proposed to use rare-earth (or lanthanide/inner transition metal) oxide ceramics as hydrophobic materials in harsh environments.
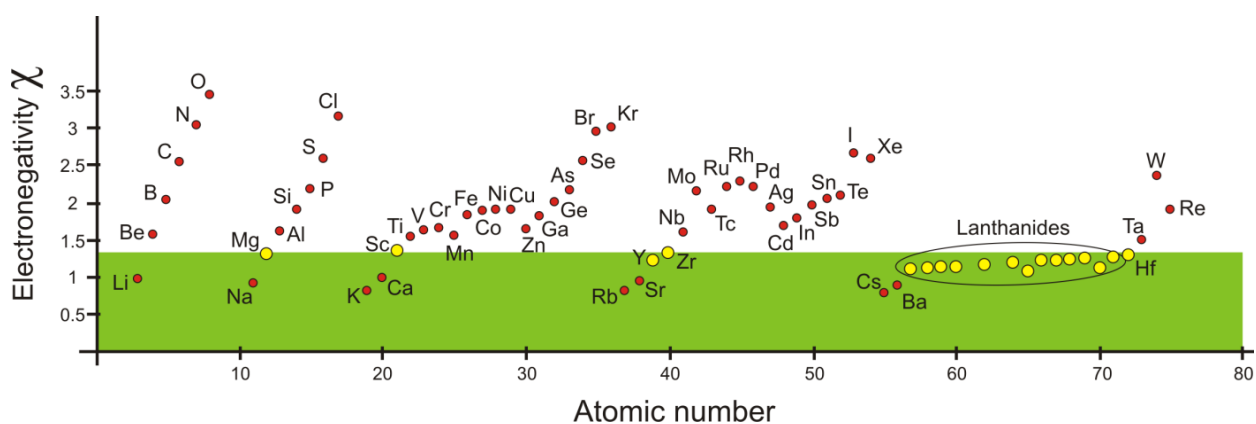
Fig.3.1 The electronegativity of elements as a function of their atomic number.

They argue that the peculiar electronic structure of these oxides leads to hydrophobicity. Specifically, the unfilled 4f orbitals of the rare-earth atoms are shielded by the full octet of electrons in the $5s^2 p^6$ shell giving these atoms a low tendency to form hydrogen bonds with nearby water molecules. Indeed, Azimi et al. [4] found experimentally that all the rare-earth oxides from cerium to lutetium are hydrophobic.

This peculiar electronic structure of the lanthanides leads to their low electronegativity, see Fig.3.1. Electronegativity of an element quantifies the tendency of an atom of that element to attract electrons.

Various electronegativity scales are being used. On the Pauling scale, defined together with the concept of electronegativity itself [3], the value of electronegativity of an element is given by the additional ionic stabilization of the bond of that element to another element compared to the two

corresponding homonuclear bonds. For all the rare earths, Fig 3.1shows that the low value of their Pauling electronegativity is between about 1.1 and 1.3. However, as Fig 3.1also shows, elements at the beginning of other periods of the periodic table have comparably low electronegativity even though they have different electronic structure, see Table 3.1.

Table 3.1 Electronic structures of metals with comparable electronegativity

Chemical element	Y	Zr	La	Nd	Hf	Mg
Electronic structure	[Kr] $4d^1\,5s^2$	[Kr] $4d^2\,5s^2$	[Xe] $5d^1\,6s^2$	[Xe] $4f^4\,6s^2$	[Xe] $5d^2\,6s^2$	[He] $3s^2$
Electronegativity (Pauling scale)	1.22	1.33	1.10	1.14	1.3	1.31

We suggest that the low value of electronegativity is more important for hydrophobicity than the mechanism by which this low value is achieved. The coordinatively unsaturated surface oxygen anions of a metal oxide act as efficient Lewis bases, and thus form hydrogen bonds with water hydrogen cations. If the coordinatively unsaturated surface metal cations have high electronegativity, they act as efficient Lewis acids, and thus form coordinate bonds with water oxygen anions.

The combined Lewis acidity and basicity of the oxide surface leads to strong interaction with water [5, 6] and thus to hydrophilic behavior with a low water droplet contact angle (WDCA) shown schematically in Fig. 3.2a. On the other hand, if the metal cations have low electronegativity, they act as poor Lewis acids, and no longer form coordinate bonds with water oxygen anions. The interaction of the oxide surface with water is therefore weakened, leading to hydrophobic behavior and an increased WDCA shown schematically in Fig. 3.2b.

The interaction of surface with water can be further weakened if we go from an oxide to a nitride, shown schematically in Fig.3.2c, as surface oxygen anions form more hydrogen bonds with water hydrogen than surface nitrogen anions. The reason is that an oxygen atom has six valence electrons out of which, in an oxide, two participate in bonding and four remain in the form of two non-bonding lone electron pairs.

On the other hand, a nitrogen atom has five valence electrons out of which, in a nitride, three participate in bonding and two remain in the form of one non-bonding lone electron pair. This difference, shown schematically in Fig.3.2d, makes nitrogen a poorer Lewis base than oxygen. To test our hypothesis, we have extended the study of Azimi et al. [4] to oxides and nitrides of other low-electronegativity metals. We have prepared all the materials in the form of thin surface films by dc reactive magnetron sputtering and measured their hydrophobicity using the sessile drop method.
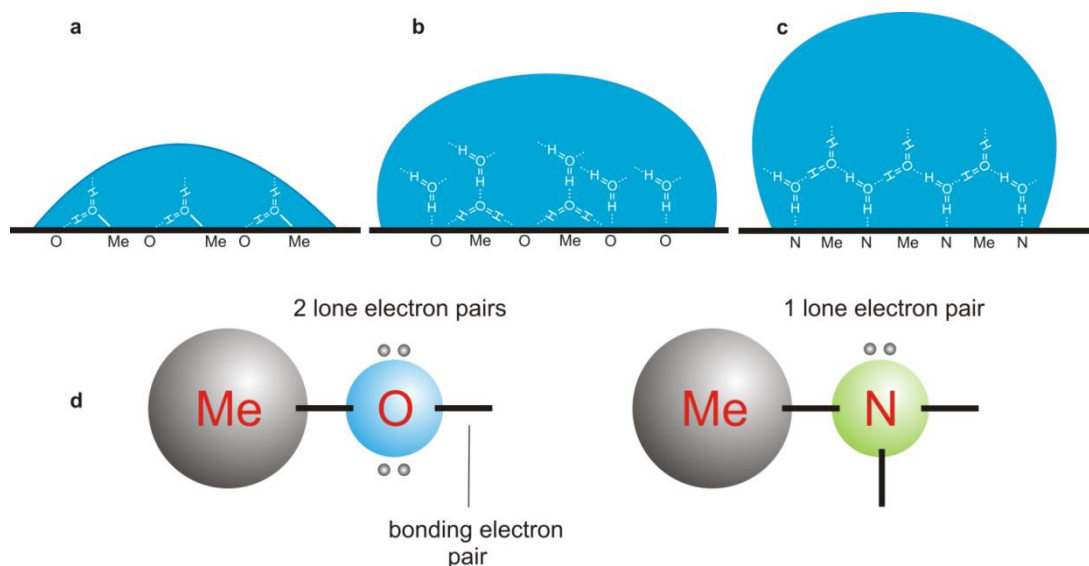
*Fig.3.2 Main principles of wetting of ceramic surfaces: **a**, Hydrophilicity of the surface of an oxide of a high-electronegativity metal. Surface oxygen anions form hydrogen bonds with water hydrogen cations and surface metal cations form coordinate bonds with water oxygen anions. Water droplet contact angle (WDCA) is lower than 90°. **b**, Hydrophobicity of the surface of an oxide of a low-electronegativity metal. Surface oxygen anions form hydrogen bonds with water hydrogen cations, but surface metal cations no longer form coordinate bonds with water oxygen anions. WDCA is around 90°. **c**, Increased hydrophobicity of the surface of a nitride of a low-electronegativity metal compared to the corresponding oxide. The number of hydrogen bonds from water hydrogen cations to the material anions is reduced by a decrease of the number of lone pairs of electrons. WDCA is further increased above 90°.**d**, Schematic of the bonding of an oxygen or nitrogen anion to a metal cation in the film. Each thick line represents a bonding electron pair. An oxygen atom contributes two of its six valence electrons to two bonding electron pairs and retains the remaining four valence electrons in the form of two lone electron pairs. A nitrogen atom contributes three of its five valence electrons to three bonding electron pairs and retains the remaining two valence electrons in the form of one lone electron pair.*

3.2 Experimental details

Films were prepared by dc reactive sputtering using a round unbalanced magnetron (UM) equipped with a Nd, Zr, La, Y or Mg target (Ø=100 mm) fixed to the UM cathode by a stainless steel ring. The reactive sputtering was carried out in a magnetron discharge sustained in an Ar+O_2 (Nd-O, La-O, Zr-O, Y-O and Mg-O) or Ar+N_2 (Nd-N, Zr-N, Y-N, La-N and Mg-N) gas mixture at a constant total pressure of sputtering gas $p_T = p_{Ar}+p_{O2}(p_{N2}) = 1$ Pa. Films were sputtered onto Si (111) substrates (20×20×0.525 mm^3 or 35×5×0.525 mm^3) under the following deposition conditions: discharge current $I_d = 0.5$ A, substrate bias $U_s = U_{fl}$, substrate temperature $T_s= 300^o$C, substrate-to-target distance d_{s-t}=60 mm with the film deposition rate a_D ranging from 9 to 13 nm/min; here U_{fl} is the floating potential. The thickness h of the films ranges from 500 to 800 nm. Roughness R_a for all prepared films ranges from 4.8 to 52 nm. The structure of the films was characterized by X-ray diffraction (XRD) using a PANalytical X'Pert PRO diffractometer. The hardness H, effective Young's modulus E^* and elastic recovery W_e were determined from load vs. displacement curves measured by a computer controller microhardness tester Fischerscope H100 equipped with a Vickers's diamond indenter at load $L = 10$ mN. The film

thickness h and surface roughness R_a were determined using the electro-mechanical Dektak 8 Stylus Profiler. Water droplet contact angle and free surface energy of the films were measured by using the Advex Instruments, s.r.o. Surface Energy Evaluation System. Hydrophobicity of the sputtered films was measured by sessile drop method with the volume of water droplet V=4µl.

3.3 Results and discussion

3.3.1 Wetting properties and surface free energy

Firstly, we prepared and studied Nd-based films to confirm the result of Azimi et al. [4] for its oxide and to check the trend of increasing hydrophobicity by comparing its oxide with its nitride. Secondly, we have studied oxides and nitrides of other low-electronegativity transition metals, namely La as the one inner transition metal not included in the Azimi et al. [4] study, and d-block transition metals Zr and Y noting that hydrophobic properties of hafnium oxides have already been reported in the literature [7-9]. Thirdly, to check that neither f- nor d- transition metal electronic structure is necessary for hydrophobicity of a low-electronegativity metal based ceramic; we prepared and studied the nitride and oxide of Mg.
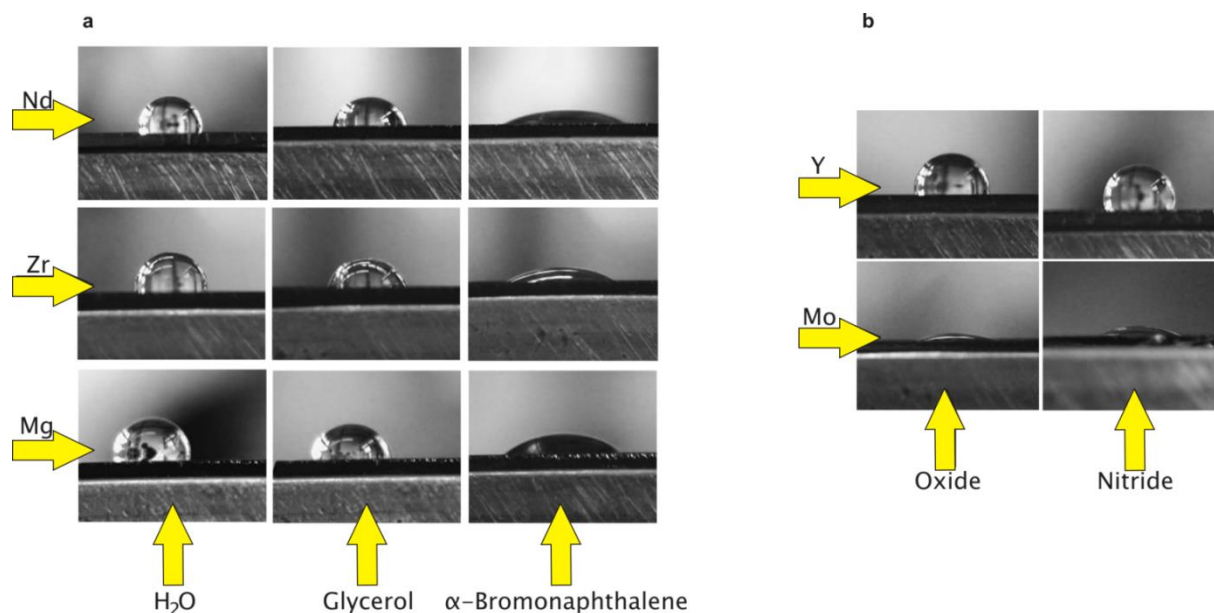
*Fig.3.3 The effect of electronegativity on hydrophobicity/hydrophilicity of material surfaces. **a**, Qualitatively same wettability of three hydrophobic oxides of low-electronegativity metals with similar values of electronegativity but different electronic structure: an inner transition metal (Nd) in the top row, a d-block transition metal (Zr) in the middle row, and a main-group metal (Mg) in the bottom row. The liquids used are decreasingly polar going from left to right: deionized water in the left column, glycerol in the middle column, and α-bromnaphthalene in the right column. **b**, Qualitatively different wettability of compounds of two d-block transition metals with different values of electronegativity. The compounds of a low-electronegativity metal (Y) in the top row are hydrophobic whereas the compounds of a high-electronegativity metal (Mo) in the bottom row are hydrophilic. The figure further shows an increased hydrophobicity of nitrides in the right column compared to oxides in the left column.*

The choice of the element here is somewhat limited by the fact that some of the bulk oxides of the alkali and alkali-earth metals dissolve in water. Lastly, to check the converse, i.e., that a high-electronegativity transition metal based ceramic is hydrophilic, we could not use an inner transition metal as they all have low electronegativity, see Fig.3.1. Instead, we used Mo as a high-electronegativity d-block transition metal. Fig.3.3 illustrates qualitatively our main results. Fig.3.3a shows very similar values of the droplet contact angles for oxides of an inner transition metal (Nd) in the top row, a d-block transition metal (Zr) in the middle row, and a main-group element (Mg) in the bottom row not just for water in the left column, but also for glycerol in the middle column and for α-bromnaphthalene in the right column. The latter two liquids are used for the evaluation of the various components of the surface free energy discussed below. From the left column we see that WDCA>90°, so all the three materials are hydrophobic, irrespective of their electronic structure. The non-polar character of all the surfaces is furthermore demonstrated by the decreasing value of the contact angle as the polarity of the liquid decreases from the left column to the right column. Conversely, Fig.3.3b shows very different WDCAs for ceramics based on two d-block transition metals with different electronegativities.

The low-electronegativity transition-metal (Y) based ceramics in the top row are hydrophobic whereas the high-electronegativity transition-metal (Mo) based ceramics in the bottom row are hydrophilic. Moreover, comparing the two columns shows the expected trend that a nitride would be more hydrophobic than a corresponding oxide. Low Lewis acidity of the surfaces of the oxides of Zr, Y, and Mg has been observed in a study of their catalytic properties [10].
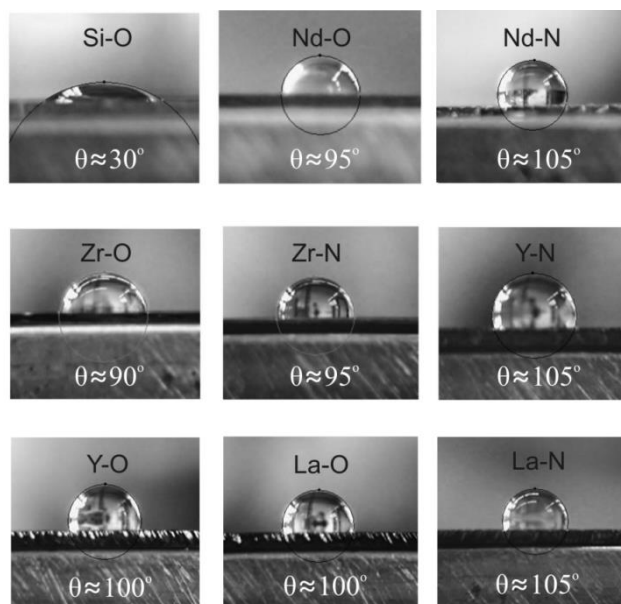
Fig. 3.4 Measurements of the water droplet contact angle (WDCA) of various surfaces. The benchmark hydrophilic surface of an oxide of Si is followed by hydrophobic surfaces of oxides of low-electronegativity inner and d-block transition metals. The material and the approximate value of WDCA are given with each image.

To quantify our results, we have calculated the non-polar Lifshitz-van der Waals γ^{LW} and the polar Lewis acid γ^{+} and Lewis base γ^{-} components of the surface free energy using the van Oss-Good-Chaudhury approach (see Supplementary Information). Fig.3.4 shows images of water

droplets and gives values of WDCA (deionized water) for a Si surface covered by the protective oxide as a benchmark hydrophilic surface followed by all the hydrophobic surfaces studied.

Table 3.2 Surface free energies of hydrophobic oxides of low-electronegativity metals. Here γ_{total} is the total surface free energy equal to the sum of the non-polar Lifshitz-van der Waals component γ^{LW} and the polar acid-base component γ^{AB}, which is given by the product of the polar Lewis acid component γ^+ and the polar Lewis base component γ^- as $\gamma^{AB}=2\sqrt{(\gamma^+ \gamma^-)}$. The polar components are about two orders of magnitude smaller than the non-polar components. For each nitride, the Lewis base component is smaller than that for the corresponding oxide.

Film Compound	γ_{total} [mJ/m^2]	γ^{LW} [mJ/m^2]	γ^{AB} [mJ/m^2]	γ^- [mJ/m^2]	γ^+ [mJ/m^2]
Nd-O	32.76	32.17	0.58	0.99	0.09
Nd-N	33.14	32.58	0.56	0.39	0.20
Zr-O	41.21	40.97	0.24	1.6	0.1
Zr-N	39.53	39.10	0.43	0.27	0.17
Y-O	27.20	26.83	0.37	0.22	0.15
Y-N	38.60	38.56	0.03	0.01	0.05
La-O	40.87	40.7	0.17	0.22	0.03
La-N	38.04	38.00	0.05	0.02	0.03
Si-O	59.00	43.72	15.29	1.74	33.53

The values of WDCA together with the values of the contact angles of drops of glycerol and α-bromnaphthalene are then used to determine the three components of the surface free energy as well as the polar acid-base component γ^{AB} (given by the product of the Lewis acid and Lewis base components as $\gamma^{AB}=2\sqrt{(\gamma^+ \gamma^-)}$, see Supplementary Information) and the total surface free energy γ_{total} given in Table 3.2. We see that for all the hydrophobic compounds, the polar component of the surface free energy is about two orders of magnitude smaller than the non-polar component so intermolecular interactions between water and surface are mostly given by electrostatic forces.

This reduced water chemical adsorption at the surface due to a reduced number of coordinate bonds then leads to higher values of WDCA in comparison with WDCA for most of metal oxides and nitrides. Furthermore, the polar Lewis base component γ^- is smaller for each nitride compared with that for the corresponding oxide, as expected.

3.3.2 Mechanical properties

To check the mechanical properties of the films, we have measured their hardness H, effective Young's modulus E^*, and elastic recovery W_e. All the values obtained are listed in Table 3.3. The film thickness h, given in the first column of Table 2, is between 500 and 800 nm for all the film investigated, which ensures the reliability of the hardness measurements. The values of hardness range from 7.8 GPa for La-N to 17.8 GPa for Zr-N, which are more than 100 times higher in comparison with the most often used fluoropolymers [11]. From Table 3.3, we also see that with a decreasing hardness H, the H/E^* ratio decreases as well, and with it also the elastic recovery.

It is worthwhile to note that the films with the ratio $H/E^* > 0.1$ exhibit high elastic recovery $W_e > 60\%$. It indicates that these films might exhibit enhanced resistance to cracking [12]. Table 3.3 also shows a weak inverse correlation between all these values and the values of WDCA, although the values of WDCA do not change much between different materials. Still, a given application might require a fine-tuned compromise between hardness and hydrophobicity.

Table 3.3 Mechanical properties of hydrophobic oxides of low-electronegativity metals. Here h (nm) stands for the film thickness, H (GPa) stands for hardness, E* (GPa) stands for the effective Young's modulus, W_e (%) stands for elastic recovery, R_a (nm) stands for surface roughness. The values of the water droplet contact angle (WDCA) are included in the last column for the sake of discussion.

Film compound	h [nm]	H [GPa]	E^* [GPa]	W_e%	H/E	R_a nm	WDCA [°]
Zr-N	720	17.8	144	73.3	0.124	4.8	94
Zr-O	770	15.7	146	69	0.108	5.6	91
Nd-N	630	13.2	119	68.9	0.111	52	108
Nd-O	800	13.1	130	67.4	0.101	40	95
Y-O	520	7.1	118	46	0.060	25	102
Y-N	620	11.1	136	56.8	0.082	5.6	106
La-O	690	11.1	138	57	0.080	7.6	100
La-N	800	7.8	128	43.2	0.060	5.8	105

3.3.3 Role of the partial pressure of the reactive gas

It is important to note that not all sputtered compounds of low-electronegativity metals show the hydrophobic effect. Contact angle for the sputtered films strongly depends on the stoichiometry and therefore on the partial pressure of the reactive gas. In Fig.3.5 dependence of water contact angle of yttrium oxide on the partial pressure of oxygen during the deposition is shown.

It is possible to divide the curve onto the 3 parts:

Part A – nonstoichiometric metal-rich yttrium oxide. The water contact angle is below 90º due to the high amount of metal which gives a high number of charged islands on the surface with an increased number of bonds with water molecules.

Part B – range of formation of stoichiometric Y_2O_3. The contact angle in this region is around 100º due to formation only hydrogen bonds between water molecules and oxygen in the film.

Part C – overstoichiometric yttrium oxide. Water contact angle is below 90º due to the ratio O/Y higher than 3/2. More details describing this effect can be found in ref. [13]
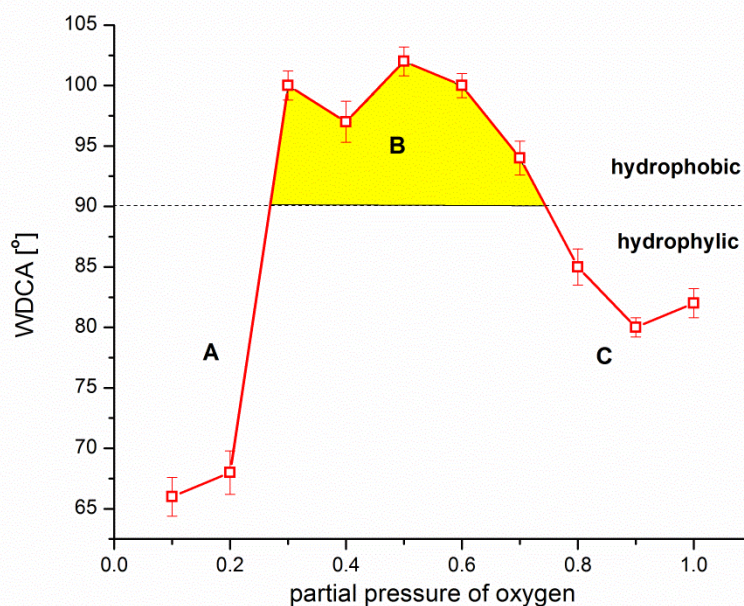
Fig.3.5 Water droplet contact angle for Y_2O_3 as a function of the partial pressure of oxygen during the deposition

3.4 Conclusions

In summary, oxides and nitrides of various low-electronegativity metals are hard hydrophobic ceramics, regardless of whether these metals are rare earths, d-block transition metals, or main-group metals. From a practical point of view, using d-block transition-metal or main-group-element based ceramics increases their application potential compared with rare-earth based ceramics, as the d-block transition metals or main-group elements are often more stable and less expensive, because they are not so "rare".

3.5 References

[1] K. Liu, L. Jiang, Nanoscale 3, 2011, 825.

[2] B.Bhushan, Y.C.Jung., Progress in Materials Science 56, 2011, 1.

[3] L. Pauling, Journal of the American Chemical Society 54, 1932, 3570.

[4] G. Azimi, R. Dhiman, H.-M.Kwon, A.T.Paxson, K.K.Varanasi. Nature Materials 12, 2013, 315.

[5] H. H. Kung. *Transition Metal Oxides: Surface Chemistry and Catal*ysis, Elsevier, 1989.

[6] V.F.Kiselev, S.N.Kozlov, A.V.Zoteev. *Fundamentals of Physics of Solid Surface*, Moscow University Publishers, Moscow, 1999, (in Russian).

[7] V.Dave, P.Dubey, H.O.Gupta, R. Chandra. Thin Solid Films 549, 2013, 2.

[8] S-S.Lin, C.-S.Liao. Surface & Coatings Technology 232, 2013, 46.

[9] R.K.Jain, Y.K.Gautam, V.Dave, A.K.Chawla, R.A.Chandra. Applied Surface Science 283, 2013, 332.

[10] H.Teterycz, R.Klimkiewicz, M.Łaniecki, Applied Catalysis A: General 249, 2003, 313.

[11] B.N.Lucas, C.T.Rosenmayer, W.C.Oliver. MRS Proceedings 505, 1997.

[12] J.Musil, Surface and Coatings Technology 207, 2012, 50.

[13] Khan S., Azimi G., Yildiz B., Varanasi K. K. Applied Physics Letters 6, 2015, 061601.

Acknowledgments

3.6 Supplementary

The van Oss-Good-Chaudhury theory of the surface free energy of solids and its components

The surface tension between a solid and a liquid, γ_{SL}, is equal to the sum of the surface tension of the solid , γ_S, the surface tension of the liquid, γ_L, and the free energy change due to the interaction of the two, ΔG_{SL},

$$\gamma_{SL} = \gamma_S + \gamma_L + \Delta G_{SL} \tag{S-e1}$$

so substitution into the Young's equation

$$\gamma_L \cos\theta = \gamma_S - \gamma_{SL} \tag{S-e2}$$

relating these surface tensions to the liquid droplet contact angle θ, gives

$$\gamma_L(1 + \cos\theta) = -\Delta G_{SL} \tag{S-e3}$$

According to the van Oss-Good-Chaudhury theory[1,2], the free energy change can be expressed as the sum of the non-polar Lifshitz-van der Waals, ΔG_{SL}^{LW}, and polar acid-base, ΔG_{SL}^{AB}, components,

$$\Delta G_{SL} = \Delta G_{SL}^{LW} + \Delta G_{SL}^{AB} \tag{S-e4}$$

and the two components of the free energy change are given in terms of the Lifshitz-van der Waals, γ_i^{LW}, Lewis acid, γ_i^+, and Lewis base, γ_i^-, components of the surface tension (*i* stands for S or L) as

$$\Delta G_{SL}^{LW} = -2\sqrt{\gamma_S^{LW}\gamma_L^{LW}}$$
$$\Delta G_{SL}^{AB} = -2\sqrt{\gamma_S^+\gamma_L^-} - 2\sqrt{\gamma_S^-\gamma_L^+} \tag{S-e5}$$

Substituting equation (S-e4) into (S-e3) with the two components of the free energy change expressed by (S-e5) gives the van Oss-Chaudhury-Good equation

$$\gamma_L(1 + \cos\theta) = 2\left(\sqrt{\gamma_S^{LW}\gamma_L^{LW}} + \sqrt{\gamma_S^+\gamma_L^-} + \sqrt{\gamma_S^-\gamma_L^+}\right) \tag{S-e6}$$

For a given solid under study, we thus have three unknown components of the surface tension, namely, γ_S^{LW}, γ_S^+, and γ_S^-, so we need three reference liquids with known values of their components of the surface tension to give us a system of three linear equations for three unknown. In this work, we used deionized water, glycerol, and α-bromnaphthalene. From the Lewis acid and Lewis base components of the solid surface tension, we can also calculate the polar acid-base component of the surface tension of the solid as

$$\gamma_S^{AB} = 2\sqrt{\gamma_S^+\gamma_S^-} \tag{S-e7}$$

Supplementary references

1. van Oss, C. J., Good, R. J. & Chaudhury, M. K. Langmuir 4, 1988, 884.

2. Good, R. J. Journal of Adhesion Science and Technology 6, 1992, 1269.

CHAPTER 4

_____

FLEXIBLE HYDROPHOBIC ZrN NITRIDE FILMS

_____

4.1 Introduction

In recent years a great attention has been devoted to the development of hydrophobic thin films and coatings, for instance, see the review papers [1-6] and investigations into some of the specific approaches [7-11]. The hydrophobicity is characterized by the water droplet contact angle (WDCA). Up to now, attention has been concentrated mainly on the search for materials with the highest value of WDCA. The highest WDCAs of ≈ 100° and higher are achieved for polymer films and coatings containing fluorine. However, the hardness H of the polymer films and coatings is low (< 5GPa) and their thermal stability is also low (less than ~300°C). These facts exclude their utilization in many applications, for instance, when the hydrophobic coatings are operated in harsh conditions such as on turbine blades or in aerospace applications. In these applications the hydrophobic coatings must be thermally stable at temperatures above 300°C, hard and exhibit enhanced resistance to cracking [12-14]. Recently, we have found that oxides and nitrides of various low-electronegativity metals exhibit an intrinsic hydrophobicity and moreover a high hardness (up to ~20 GPa) and a high thermal stability (~ 1000°C and more). More details are given in Ref. [15]. However, up to now, there is no report on the flexibility of the hydrophobic coatings, which is of a key importance when such coatings are operated on flexible substrates and can crack. Therefore, this paper reports on the development of the flexible hydrophobic ZrN nitride films resistant to cracking. The ZrN nitride films are typical representatives of carbon-free low-electronegativity metal compounds with (i) weak bonds with water, i.e. with a strong hydrophobic effect, and (ii) mechanical properties resulting in their enhanced resistance to cracking.

4.2 Experimental details

The stoichiometric ZrN films were reactively sputtered using a round unbalanced magnetron equipped with a Zr target of diameter 100 mm in an Ar + N$_2$ gas mixture at total pressure $p_T = p_{Ar} + p_{N2} = $ 1Pa and $p_{N2} = $ 0.4Pa. The magnetron was powered by a DC power supply. The films were sputtered onto Si (100) substrates (20 x 20 x 0.525 mm^3 and 35 x 5 x 0.525 mm^3) and a Mo strip (50 x 15 x 0.1 mm^3) under the following deposition conditions: discharge current $I_d = $ 0.5A, substrate bias $U_s = U_{fl}$, -35V, -50V, -65V and -80V, $U_{fl} = $ -23 V, substrate temperature $T_s = $ 300°C, and substrate-to-target distance $d_{s-t} = $ 60 mm, with a resulting deposition rate of coatings $a_D \approx$ 10 nm/min; here U_{fl} is the floating potential. The thickness h of the coatings ranges from ~ 1500 to ~ 2000 nm. The film thickness h and the surface roughness R_a were determined using the electro-mechanical stylus profilometer (Dektak 8 Stylus Profiler, VEECO, Plainview, NY). The structure of the films was characterized by X-ray diffraction (XRD) using a diffractometer (X'Pert PRO; PANanalytical, ALMELLO, the Netherlands). The hardness H, effective Young's modulus E^* and elastic recovery W_e of films were determined from load versus displacement curves measured by a computer-controlled microhardness tester (Fischerscope H100 VP XY PROG, Windsor, CT) equipped with a Vickers diamond indenter at load $L = $ 10 mN. The surface morphology of bent films deposited on Mo strips was investigated by an optical microscope and the fracture cross sections of films deposited on Si (100) substrates was investigated by a Hitachi SU-70 scanning electron microscope (SEM). The water droplet contact angle (WDCA) of the films was measured by the Drop Shape Analyzer DSA30, KRUSS GmbH. The hydrophobicity of sputtered films was measured by the sessile drop method with the volume of water droplet $V = $ 2 μl. The resistance of films to cracking was characterized by (i) the

bending test (the Mo strip coated with the sputtered film was bent around a fixed cylinder of radius r =5 mm) and (ii) the indentation test at a high diamond indenter load L (the impression of the diamond indenter in the surface of film at a high load L = 500 mN); more details are given in the reference [14].

4.3 Results and discussion

4.3.1 Mechanical properties

Recently it was found that coatings with a high ratio $H/E^* > 0.1$, a high elastic recovery $W_e > 60\%$ and compressive macrostress ($\sigma < 0$) are flexible and exhibit an enhanced resistance to cracking [12,13]. On the other hand, coatings with a low ratio $H/E^* < 0.1$, a low elastic recovery $W_e < 60\%$ and tensile macrostress ($\sigma > 0$) are brittle and easily crack [12, 13]. We will show here (data in Fig. 4.1 and Tables 4.1 and 4.2) that hydrophobic ceramic films are no exception to this principle. It means that the flexibility/brittleness of the hydrophobic films can be controlled by their mechanical properties.

The evolution of the hardness H, effective Young's modulus E^* and macrostress of the sputtered ZrN films with increasing substrate bias U_s is displayed in Fig.4.1. From this figure it is seen that (i) only the ZrN films sputtered at high negative substrate biases ($|U_s| > 50$ V) can exhibit an enhanced resistance to cracking due to a high ratio $H/E^* > 0.1$ and a high elastic recovery $W_e > 60\%$, see Table 4.1, and (ii) all ZrN films exhibit compressive macrostress ($\sigma < 0$), which increases with increasing U_s. The increase of the negative substrate bias above -80 V is limited by the increase of compressive macrostress σ in the film because of its delamination from the substrate. The decrease of the coating hardness H with increasing bias up to -50 V is caused by re-sputtering of the nitrogen atoms from the surface of growing film by bombarding ions and the formation of slightly substoichiometric $ZrN_{x<1}$ coatings with the stoichiometry x = N/Zr < 1 decreasing with increasing negative substrate bias U_s; for more details see, for instance, Ref. [16] where the desorption process of N atoms from the surface of sputtered film induced by ion bombardment was investigated in details. The decrease of the hardness H with decreasing stoichiometry x below 1 is well known fact. When the negative bias U_s is increased above -50 V the energy E_{bi} delivered into the growing coating strongly increases. It is a reason why the hardness H of coatings increases with increasing negative bias above -50V.¨

Here, it is also worthwhile to note that the mechanical properties of the film are controlled by the energy E delivered into the film during its growth. This energy E is a result of combination of the deposition parameters used in the formation of the film. Under the deposition conditions used, E ≈ E_{bi}, where E_{bi} is the energy delivered into the film by bombarding ions. The energy E_{bi} can be easily controlled by the substrate bias U_s, the substrate ion current density i_s and the deposition rate a_D of film. The energy E_{bi} increases with increasing (i) negative substrate bias U_s and (ii) substrate ion current density i_s and with decreasing deposition rate a_D according to the formula $E_{bi} \approx U_s\, i_s/a_D$. In our experiment the energy E_{bi} was controlled by the negative substrate bias U_s.
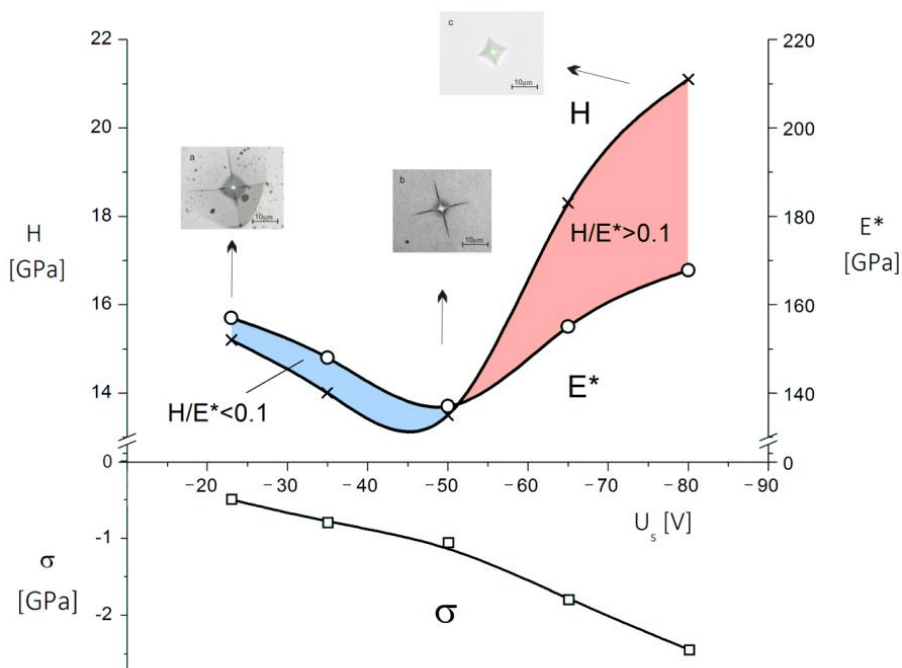
Fig.4.1 Hardness H, effective Young's modulus E^* and macrostress σ of the ZrN films as a function of the substrate bias U_s.

4.3.2 Resistance of flexible and brittle films to cracking

The resistance of the film to cracking was assessed using two methods: (1) the indentation test and (2) the bending test; more details are given in the reference [14]. In the indentation test a diamond indenter is impressed in the surface of a film deposited on a Si (100) substrate at a high load $L \geq 0.25$ N increasing up to its cracking.

Table 4.1 Physical and mechanical properties of ZrN nitride films sputtered on Si(100) substrate held at a floating ($U_s = U_{fl}$) and negative bias ($U_s < 0$). Mechanical properties were measured at a low diamond indenter load L = 10 mN.

Film	U_s [V]	i_S [mA/cm^2]	h [nm]	a_D [nm/min]	E_{bi} [MJ/cm^3]	H [GPa]	E^* [GPa]	H/E^*	σ [GPa]
1	U_{fl}	0	1655	9.2	~ 0	15.2	157	0.096	-0.5
2	-35	0.08	1780	9.9	0.17	14.4	148	0.095	-0.8
3	-50	0.11	1600	8.9	0.37	13.5	137	0.098	-1.1
4	-65	0.20	1850	10.3	0.76	18.3	155	0.118	-1.8
5	-80	0.38	1940	10.8	1.69	21.1	169	0.125	-2.4

Now, it is necessary to demonstrate that the ZrN films with a high ratio $H/E^* \geq 0.1$ and a high elastic recovery $W_e > 60\%$ really exhibit the enhanced resistance to cracking.

The results of this test are summarized in Fig. 4.2. Three ZrN films with different mechanical properties were tested at the same high load $L = 0.5$ N. As expected, from Fig. 4.2 it is clearly seen that while the ZrN films with a low ratio $H/E^* < 0.1$ and a low elastic recovery $W_e < 60\%$ easily crack, the ZrN films with a high ratio $H/E^* > 0.1$ and a high $W_e > 60\%$ exhibit no cracks. It confirms that only the ZrN films with a high ratio $H/E^* > 0.1$ and a high $W_e > 60\%$ exhibit the enhanced resistance to cracking.
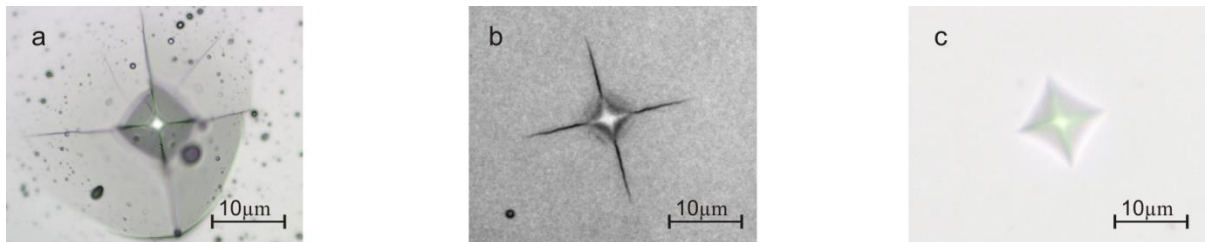
Fig.4.2 Photos of Optical Microscope images of the diamond indenter imprints in the surface of the ZrN films, sputtered at (a) $U_s = U_{fl}$ (the film No.1), (b) $U_s = -50$ V (the film No.3) and (c) $U_s = -80$ V (the film No.5), at the load $L = 0.5$ N.

The same result is obtained also by the bending test. In the bending test the ZrN film is deposited on the Mo strip and the coated Mo strip is bent around a fixed cylinder of the radius r. In this test the tested film is alongated and its prolongation increases with decreasing radius r of the fixed cylinder. The same ZrN films as in the indentation test were used. In this test a fixed cylinder with the radius $r = 5$ mm was used. The results of this test are given in Fig.4.3. The bending test also confirms that only the ZrN films with high ratio $H/E^* > 0.1$ and high $W_e > 60\%$ exhibit the enhanced resistance to cracking. The results of both the indentation and bending test are summarized in Table 4.2.

Fig.4.3 Photos of Optical Microscope images of surface morphology of the ZrN films, sputtered on Mo strip at (a) $U_s = U_{fl}$ (the film No.1), (b) $U_s = -50$ V (the film No.3) and (c) $U_s = -80$ V (the film No.5), after bending around fixed cylinder of radius $r = 5$ mm. The photos were taken under load.

From both tests it can be concluded that (1) only the ZrN films with high ratio $H/E^* > 0.1$ and high $W_e > 60\%$ exhibit the enhanced resistance to cracking and (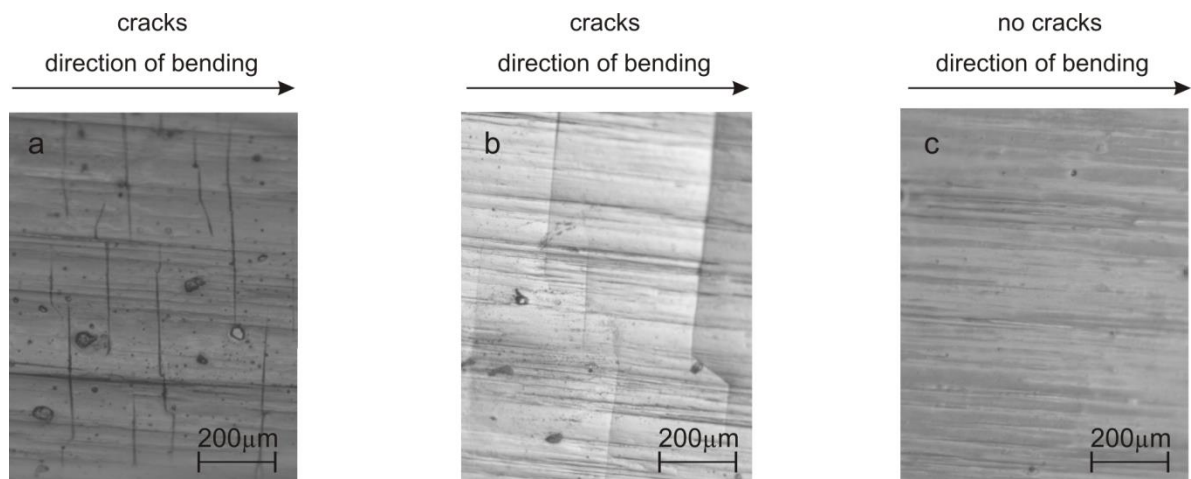2) both the indentation and bending test (i) give the same results and (ii) can be used to characterize the resistance of the film to cracking.

Table 4.2 Resistance to cracking and hydrophobicity of the ZrN nitride films sputtered on Si(100) substrate held at floating ($U_s = U_{fl}$) and negative bias ($U_s < 0$). Values E_{bi}, W_e, H/E^*, and σ are given for correlations with mechanical properties of the film.

Film	U_s [V]	E_{bi} [MJ/cm^3]	W_e [%]	H/E^*	σ [GPa]	R_a [nm]	WDCA [°]	cracks indentation[x]	bending[xx]
1	Ufl	~ 0	60	0.096	-0.5	81	98	yes	yes
2	-35	0.17	62	0.095	-0.8	16	95	yes	yes
3	-50	0.37	53	0.098	-1.1	6	94	yes	yes
4	-65	0.76	77	0.118	-1.8	10	94	no	no
5	-80	1.69	75	0.125	-2.4	12	93	no	no

R_a is the surface roughness of ZrN films sputtered on polished Si (100) substrate, [x] indentation at $L = 0.5$ N, [xx] bending around cylinder of radius $r = 5$ mm.

Very important characteristic of every film is its fracture cross section microstructure. The images of fracture cross section of the ZrN films sputtered at (a) $U_s = U_{fl}$ = -23 V (the film No.1), (b) U_s = -50 V (the film No.3) and (c) U_s = -80 V (the film No.5) are displayed in Fig.4.4. All coatings exhibit a columnar microstructure and compressive macrostress ($\sigma < 0$). The columnar microstructure correlates well with a strong ZrN (111) preferred crystallographic orientation of all these films, see Fig.4.6.

a)   b)   c)
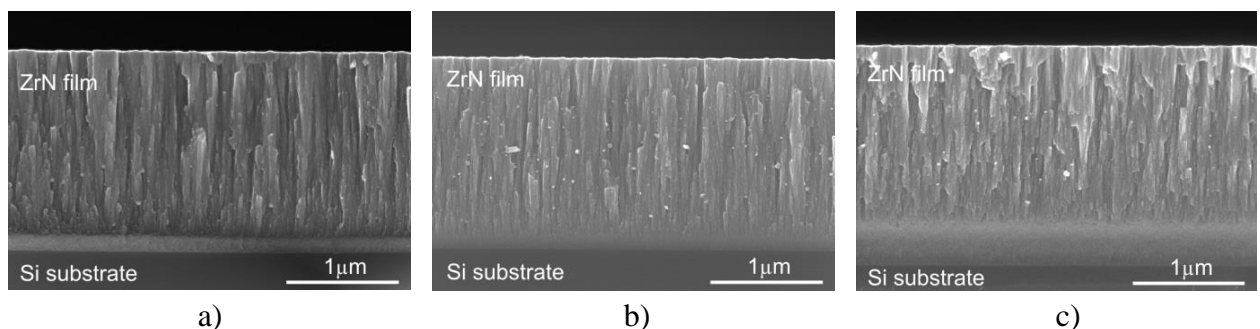
Fig.4.4 Photos of SEM fracture cross sections images of the ZrN films, sputtered on Si (100) substrates at (a) $U_s = U_{fl}$ (the film No.1), (b) U_s = -50 V (the film No.3) and (c) U_s = - 80 V (the film No.5).

However, here, it is worthwhile to note that the films with columnar microstructure exhibit an enhanced resistance to cracking only in the case when a sufficient energy E_{bi} is delivered to them during their growth, see Table 4.2.

4.3.3 Hydrophobicity of ZrN films

The hydrophobicity of the sputtered ZrN films is characterized by a high WDCA of about 95°, see Fig.4.5. This figure compares the WDCA on the surface of (a) a pure Si wafer and (b) a ZrN film sputtered on a pure Si wafer.
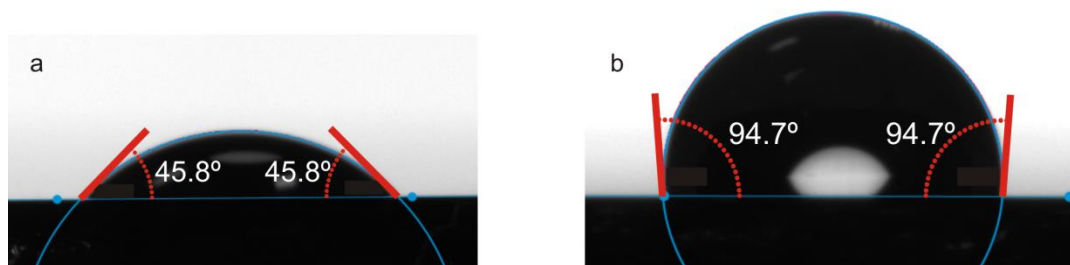
Fig.4.5 Photos of optical microscope images of WDCA on (a) pure Si substrate and (b) ZrN film sputtered on Si substrate.

As can be seen from Tables 4.1 and 4.2 the hydrophobicity of the sputtered ZrN films does not depend on their mechanical properties (H, E^*, W_e and H/E^* ratio) and the energy E_{bi} delivered to the film during its growth. Since the energy E_{bi} affects the structure of the film, the hydrophobicity does not depend on the structure either, see Fig.4.6 and Table 4.2. It means that all sputtered ZrN films exhibit hydrophobic properties. Fig.4.6 also shows that the XRD patterns of sputtered ZrN films exhibit a relatively broad low-intensity XRD response. This broad low intensity shoulder at 32° 2Θ is a result of the presence of an amorphous phase of zirconium oxide in sputtered films.

Fig.4.6 Evolution of XRD patterns of ZrN films with increasing negative substrate bias U_s. All ZrN films were deposited on the substrates made of Si (100) wafers.

The zirconium oxide is probably formed in a reaction of the sputtered Zr atoms with oxygen O atoms from a residual atmosphere in the deposition chamber because in our experiment the base pressure p_0 in our deposition chamber is relatively high (the deposition chamber is evacuated by an oil dif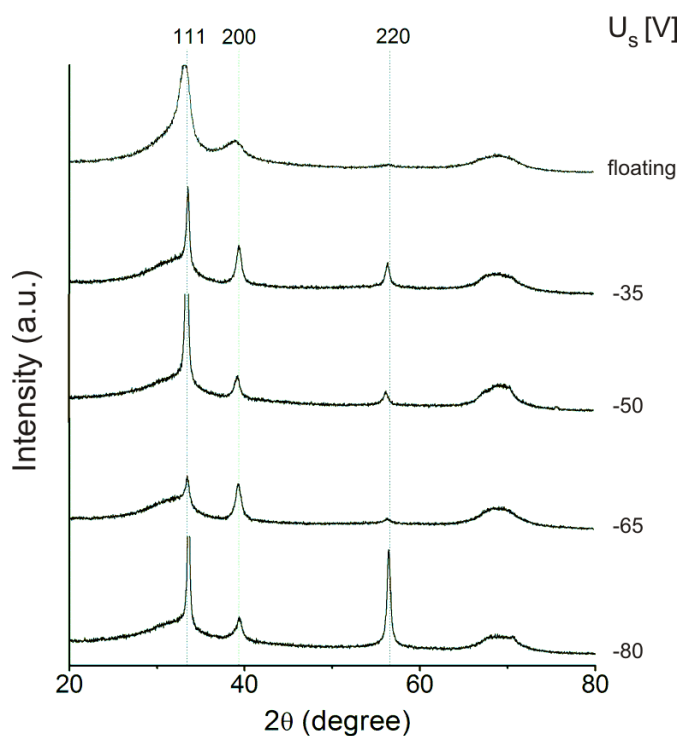fusion pump to $p_0 \approx 3 \times 10^{-3}$ Pa only) and the film deposition rate is relatively low ($a_D \approx 10$ nm/min). The higher p_0 and the lower a_D are, the higher is also the contamination of the film by oxygen; for more details see Ref. [17].

The hydrophobicity is an intrinsic property of the low-electronegativity metal compounds, see Fig. 4.7. All open points denote the elements whose compounds, for instance nitrides and oxides, exhibit intrinsic hydrophobicity. This fact was confirmed experimentally and obtained results are reported in Refs. [15], [18], [19], [20] and [21].
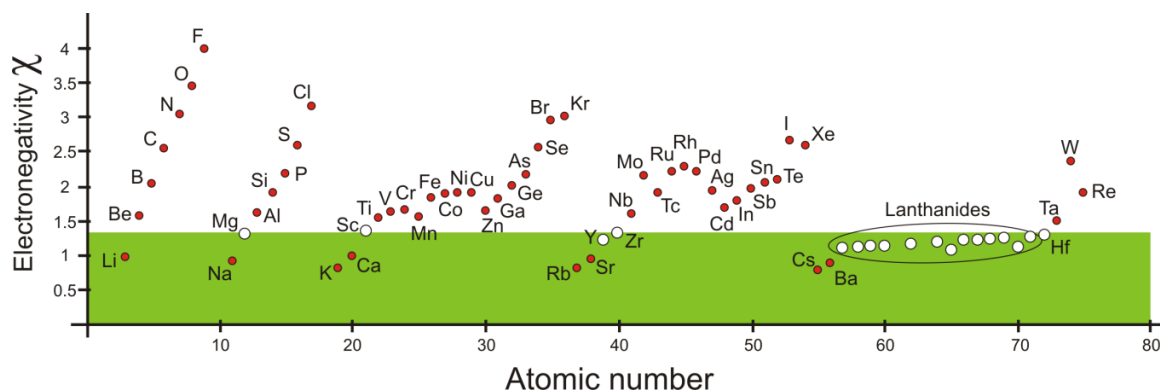

Fig. 4.7 The electronegativity of elements as a function of their atomic number. Adapted after Ref. [15].

As can be seen from Table 4.2 the hydrophobicity of the sputtered ZrN film slightly depends on the roughness of its surface. The WDCA is slightly decreased by the application of the negative substrate bias due to the smoothening of film surface under an increased ion bombardment in agreement with the Wenzel equation [22].

4.4 Conclusions

This article reports on sputtering of the hydrophobic ZrN nitride films with enhanced resistance to cracking. It is shown that

1. The hydrophobicity of the ZrN nitride film is its intrinsic property due to the low-electronegativity of Zr and does not depend on its mechanical properties and structure. Therefore, all sputtered ZrN films are hydrophobic.

2. The enhanced resistance to cracking of the ZrN film must be optimized by its mechanical properties. It was found that only the ZrN films with high ratio $H/E^* > 0.1$, high elastic recovery $W_e > 60\%$ and compressive macrostress $|\sigma| > 1$ GPa exhibit an enhanced resistance to cracking. These films can be created only in the case when a sufficient energy E_{bi} is delivered to the growing film. It means that not all sputtered hydrophobic ZrN films exhibit the enhanced resistance to cracking.

3. The hydrophobic ZrN films with enhanced resistance to cracking can be prepared by the optimization of their mechanical properties only. The mechanical properties of the film can be effectively controlled by the energy E_{bi} delivered into film during its growth by bombarding ions.

4. The hydrophobic ZrN films with enhanced resistance to cracking can be used as carbon-free protective coatings in harsh environments.

Acknowledgement

4.5 References

[1] B. L. Feng, S. Li, Y. Li, H. Li, L. Zhang, J. Zhai, Y. Song, B. Liu, L. Jiang, and D. Zhu, Advanced Materials 14, 2002, 1857.

[2] D. Que´re´, Annual Review of Materials Research 38, 2008, 71.

[3] F. Xia, Y. Zhu, L. Feng and L. Jiang, Soft Matter 5, 2009, 275..

[4] B.Bhushan, Y.C.Jung. Progress in Materials Science 56, 2011, 1.

[5] S.S.Latthe, A.B.Gurav, C.S.Maruti, R.S.Vhatkar, Journal of Surface Engineered Materials and Advanced Technology 2, 2012, 76.

[6] T. Dey, D. Naughton, Journal of Sol-Gel Science and Technology 77, 2016, 1.

[7] D. Chandler, Nature 437, 2005, 640.

[8] Y. Lu, S. Sathasivam, J. Song, C. R. Crick, C. J. Carmalt, I. P. Parkin, Science 347, 2015, 1132.

[9] J. Rafiee, X. Mi, H. Gullapalli, A. V. Thomas, F. Yavari, Y. Shi, P. M. Ajayan, N. A. Koratkar, Nature Materials 11, 2012, 217.

[10] C. Shih, Q. H. Wang, S. Lin, K. Park, Z. Jin, M. S. Strano, and D. Blankschtein, Physical Review Letters 109, 2012, 176101.

[11] Q. Wei , C. Schlaich , S. Prévost , A. Schulz , C. Böttcher ,M. Gradzielski , Z. Qi , R. Haag , and C. A. Schalley, Advanced Materials 26, 2014, 7358.

[12] J.Musil, Surface and Coatings Technology 207, 2012, 50.

[13] J.Musil, RSC Advances 5, 2015, 60482.

[14] J.Musil, *Advanced hard coatings with enhanced toughness and resistance to cracking, Chapter 7 in the book Thin Films and Coatings. Toughening and Toughness Characterization,* S.Zhang (Editor), CRC Press, USA, 2015.

[15] S.Zenkin, S.Kos, J.Musil, Journal of the American Ceramic Society 97, 2014, 2713.

[16] J.Musil, R.Daniel, Surface and Coatings Technology 166, 2003, 243.

[17] P.Pokorný, J.Musil, P.Fitl, M.Novotný, J.Lančok, J.Bulíř, Plasma Processes and Polymers 12, 2015, 416.

[18] G.Azimi, R.Dhiman, H.-K.Kwon, A.T.Paxson, K.K.Varanasi, Nature Materials 12, 2013, 315.

[19] I. Oh, K. Kim, Z. Lee, K. Y. Ko, C. Lee, S. J. Lee, J. M. Myung, C. Lansalot-Matras, W. Noh, C. Dussarrat, H. Kim, and H. Lee, Chemistry of Materials 27, 2015, 148..

[20] R.K. Jain, Y. K. Gautam, V. Dave, A. K. Chawla, R. Chandra, Applied Surface Science 283, 2013, 332.

[21] S. Lin, C. Liao, Applied Surface Science, 2016, in press.

[22] R.N.Wenzel, Industrial & Engineering Chemistry 28, 1936, 988..

CHAPTER 5

_____

THICKNESS DEPENDENCE OF WETTING PROPERTIES AND SURFACE FREE ENERFY OF HfO$_2$ THIN FILMS

_____

5.1 Introduction

There has been a considerable effort to develop hydrophobic ceramics that would combine high hardness, excellent thermal stability, and wear resistance with values of water droplet contact angle (WDCA) close to those for organic- and fluoro-polymers. This combination is desirable for robust hydrophobic surfaces in harsh-environment applications such as dropwise condensation heat transfer [1, 2] or stable anti-ice protective coatings [3]. In these applications polymers do not have the required thermal properties and surface patterning giving rise to (super)hydrophobicity [4,5] would be destroyed mechanically, so hydrophobicity intrinsic to the ceramic is required. Recently, Azimi et al. reported their finding that lanthanide oxides are intrinsically hydrophobic ceramics [6].
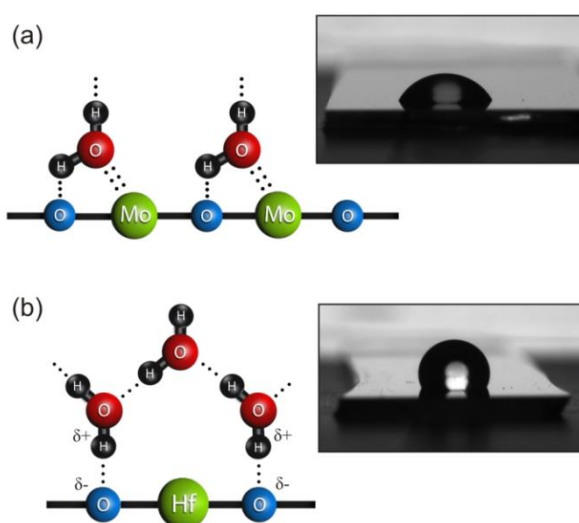

Fig. 5.1 Schematic illustration of water molecules on a hydrophilic and a hydrophobic surface: a) a high-electronegativity metal oxide, for example, molybdenum oxide forms a high number of strong coordinate bonds with water oxygen in addition to hydrogen bonds between water hydrogen and surface oxygen and therefore shows a low value of the contact angle with water; b) a low-electronegativity metal oxide, for example, hafnium dioxide forms only hydrogen bonds between surface oxygen and water hydrogen and exhibits a high value of contact angle with water.

The authors attribute the intrinsic hydrophobicity to the screening of the incompletely filled 4f shell characteristic for the lanthanides, which leads to a reduced interaction between water molecules and the oxide surface. However, in our subsequent work [7] we suggested that the underlying principle at work here is the low electronegativity of the metal cation irrespective of whether it was achieved by the screening of 4f electrons or by some other mechanism. Indeed, we found there that other low-electronegativity metals such as magnesium from the main group and zirconium, yttrium, or hafnium from the d-block of the periodic table can form hard hydrophobic oxides and nitrides with WDCA comparable with those for lanthanide oxides.

These findings were also confirmed by the works [8, 9] for HfO_2 and [10] for Y_2O_3. Schematically, interactions of water with a high- (molybdenum) and a low- (hafnium) electronegativity metal oxide are shown in Fig.5.1. An oxide of molybdenum forms a high number of strong co-ordinate bonds with water molecules in addition to hydrogen bonds between

surface oxygen and water hydrogen and exhibits strong wetting by water, see Fig.5.1a. Conversely, an oxide of hafnium forms only hydrogen bonds with water hydrogen without any strong bonds between surface hafnium and water oxygen giving rise to a reduced wetting by water, see Fig.5.1b.

Due to the fact that interactions of water with low-electronegativity metal oxide are $\approx 99\%$ electrostatic in nature [6, 7], we expect a strong dependence of wetting properties on the thickness of the film. A similar effect has been observed for van der Waals solids such as graphene [11, 12] and molybdenum disulfide [13]. Also, size-dependent surface free energy has been reported for TiO_2 nanoparticles [14]. It has the potential to increase WDCA above the intrinsic bulk value by reducing the film thickness. To confirm our prediction we selected the already insinuated hafnium dioxide as a representative compound of a low-electronegativity metal, which previously was well studied due to its high dielectric constant, high melting point and transparency [15]. To prepare dense homogeneous stoichiometric HfO_2 films with smooth surfaces and well controlled thickness down to the units of nm, we used the reactive high-power impulse magnetron sputtering (HiPIMS) with a pulsed reactive gas flow control (RGFC). In HiPIMS [16-19] highly ionized fluxes of particles onto substrates with high fractions of metal ions and enhanced energies with which the ions bombard the substrate surface [20] allow the growth of dense homogeneous oxide films [16]. Specifically HfO_2 thin films have already been prepared by HiPIMS [21-23]. Our RGFC method is able to utilize the exclusive benefits [18] of the HiPIMS discharge to maintain a sputter deposition of stoichiometric robust films.

Due to the experimental conditions used we could neglect the effect of other factors that could potentially influence hydrophobic properties of metal ceramics such as surface metal/anion ratio [24] (films were stoichiometric), surface roughness [4], amount of hydrocarbon impurities [25] (values of contact angles were the same within a few minutes after the deposition and several months later), number of adsorption centers on the surface [26] (Hf is a poor Lewis acid), and sort of the surface anion [7] (oxide only). These factors will be discussed further below.

5.2 Experimental details

The films were deposited using a strong unbalanced magnetron source with a directly water-cooled planar hafnium target (99.9% Hf purity, a diameter of 100 mm and a thickness of 6 mm) in a standard stainless-steel vacuum chamber (a diameter of 507 mm and a length of 520 mm), which was evacuated by a diffusion pump backed up with a rotary pump. The base pressure before deposition was 10^{-3} Pa. The magnetron was driven by a high-power pulsed dc power supply (HMP 2/1, Hüttinger Elektronik). For all films in this work, the repetition frequency was 500 Hz and the voltage pulse duration 200 µs with the corresponding duty cycle 10 % and the deposition-averaged target power density was 15 Wcm^{-2}. A very high deposition rate 90 nm/min and further experimental details are discussed in [21]. Depositions were performed using the feed-back pulsed O_2 flow control [18]. The film thickness was controlled by the time of the deposition. The film thickness was measured at the film edge by profilometry (Dektak 8 Stylus Profiler, Veeco) using a 380 µm thick removable Si step, and at various places of the film by ellipsometry (VASE) using a J.A. Woollam Co. Inc. instrument. The maximum measurement error of both of these techniques was well below 1%. The position of the film edge at the substrate holder was the same in all the depositions with the center of the film edge 10 mm from the axis. X-ray diffraction (XRD) measurements were carried out at room temperature on a

PANalytical X'Pert PRO diffractometer working in the Bragg–Brentano geometry using a CuKα (40 kV, 40 mA) radiation. To avoid a strong reflection from the Si (100) substrate, a slightly asymmetrical diffraction geometry with an ω-offset of 1.5° was used. Samples were scanned over the 2θ-range from 8° to 108°. Water spectra were determined by a FTIR Spectrometer NICOLET 380 in conjunction with an attenuated total reflection accessory (ATR). A thin film of water was added to the surface of each HfO_2 film and this combined water-HfO_2 layer was scanned with the depth of penetration 670nm. The surface morphology of the films was determined by atomic force microscopy (AFM) using a SmartSPM Microscope (AIST-NT) with a silicon tip (nominal radius of 10 nm) in a non-contact mode and Hitachi SU-70 scanning electron microscope (SEM). WDCA, surface free energy of the films and their Lifshitz-van der Waals and acid-base components were measured by using the Drop Shape Analyzer DSA30, KRÜSS GmbH. The wetting properties of the sputtered HfO_2 films were measured by the sessile drop method with the volume of water droplet $V = 2\mu l$. For determination of the surface free energy components we used three testing liquids: deionised water, glycerol and 1-bromonaphtalene.

5.3 Results

HfO_2 films were deposited with various thicknesses from 50nm to 250nm with the step of 50nm. For comparison, a 2300 nm-thick film was deposited and regarded as bulk HfO_2. Fig. 5.2 shows main differences in XRD patterns, SEM images and WDCA between 100 nm and 2300 nm-thick HfO_2 films. All films exhibited a nanocrystalline structure with a dominant monoclinic phase (m-HfO_2, Card No. 34-0104 in Ref. [27]) with a preferred (-1 1 1) orientation at $2\Theta = 27.90°$, with a non-dominant (0 0 2) orientation at $2\Theta = 35.53°$ and with asymmetry of the m-HfO_2 (-1 1 1) diffraction peak indicating a possible presence of a small amount of the tetragonal phase (t-HfO_2, Card No. 8-0342 in Ref. [27]) in the films. The left panels of Fig. 5.2 show XRD patterns for 100nm and 2300nm thick HfO_2 films with these features. For both films, the crystal grain sizes were about 5-7 nm. The higher peak intensities in the lower panel are due to the higher film thickness. The SEM images for the same 100nm and 2300nm thick HfO_2 films are shown in the middle panels of Fig.5.2. All films were smooth and with homogeneous surface topography. The values for the average roughness, measured by AFM, profilometer and ellipsometry, were practically the same and less than 8nm for all films. This small value of film roughness gives a negligible effect on the value of the contact angle [4]. For the films of our primary interest with the lowest thickness of 50nm exhibiting the highest contact angle, the roughness of 5nm combined with the particle size of 30nm gives an increase of the true area compared to the apparent area by the factor r estimated by $\sqrt{(15^2+5^2)}/15 \approx 1.05$ giving rise, according to the Wenzel equation $\cos\theta^* = r\cos\theta$ with $\theta^* \approx 120°$, to the change of the water droplet contact angle from θ^* to θ of about 1 degree. Also, films of thicknesses from 50nm to 250nm were densified as demonstrated by a high value of the refractive index (at the wavelength of 550nm) of 2.04. In parallel, the very low value of the extinction coefficient (at the wavelength of 550nm) of not more than 0.7×10^{-3} proved that the films were stoichiometric. The values for the bulk material and a detailed review of optical constants for HfO_2 films can be found in [26]. The right panels of Fig. 5.2 illustrate our main result: WDCA for the 2300 nm thick film $\theta_{2300} \approx 100°$ is significantly lower than that for the 100 nm thick film $\theta_{100} \approx 120°$.

For deeper understanding of the dependence of HfO_2 wetting properties on the thickness of the film we use the van Oss - Good - Chaudhury equation [28]:

$$\gamma_L(1+\cos\theta) = 2\left(\sqrt{\gamma_S^{LW}\gamma_L^{LW}} + \sqrt{\gamma_S^+\gamma_L^-} + \sqrt{\gamma_S^-\gamma_L^+}\right)$$

Here θ is the contact angle with a droplet of liquid L, γ_S^{LW} is the electrostatic Lifshitz-van der Waals component of the surface free energy of the solid film, and γ_S^+ and γ_S^- are, respectively, the polar Lewis acid and the polar Lewis base components giving the polar acid-base component γ_S^{AB} as:

$$\gamma_S^{AB} = 2\sqrt{\gamma_S^+\gamma_S^-}$$

The total surface free energy of the solid film γ_S is then given as the sum of the electrostatic Lifshitz-van der Waals and the polar acid-base component:

$$\gamma_S = \gamma_S^{LW} + \gamma_S^{AB}$$

The corresponding components of the surface free energy of the droplet forming liquid are denoted with the subscript L. Fig. 5.3a shows that the surface free energy of HfO_2 films decreases with a decreasing thickness of the film.
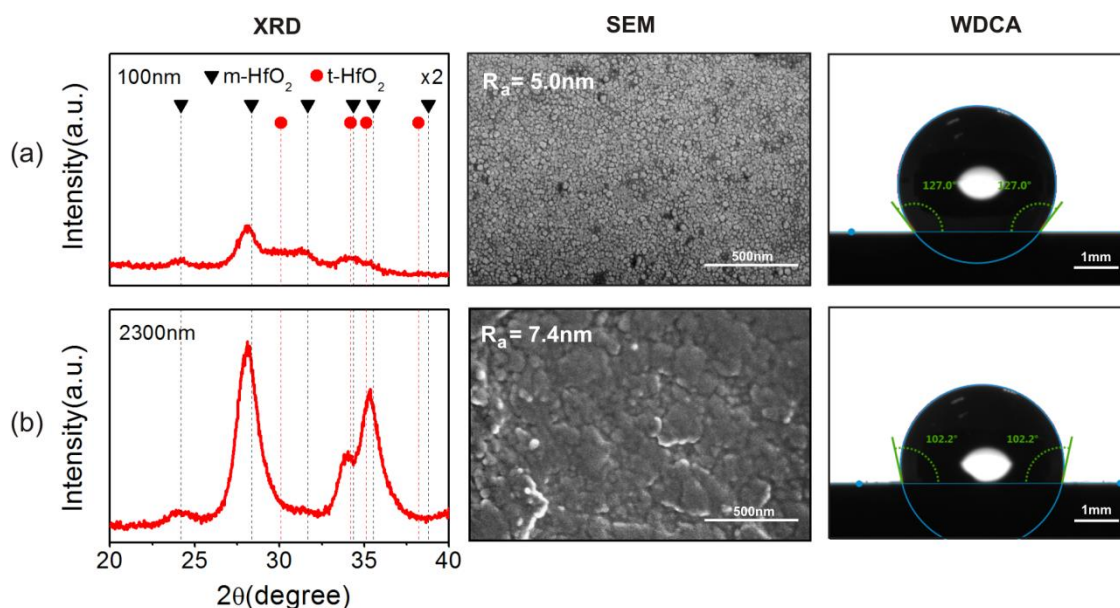
Fig.5.2 XRD patterns, SEM images of the surface and images of water droplets with indicated values of WDCA for a) 100nm thick film and; b) 2300nm thick film.

For all films, values of the electrostatic Lifshitz – van der Waals component are close to the values of the total surface free energy. As the total surface free energy decreases from $\gamma_{bulk} \approx 33mJ/m^2$ for the bulk HfO_2 to $\gamma_{100} \approx 26mJ/m^2$ for the 100nm-thick film, WDCA increases correspondingly up to 120º. A decrease of the film thickness below 50nm does not lead to a further increase of WDCA nor to a further decrease of the surface free energy. Orientation of the water molecules on the surface was measured by the FTIR-ATR technique. The normalized FTIR spectrum for the 100nm film is shown in Fig. 5.3b. The total OH-stretching absorption peak of water (dashed line) was divided [6, 29, 30] into three peaks: the ~3200cm^{-1} peak

attributed to the strongly H-bonded or tetrahedrally coordinated bulk water (red), the ~3400cm^{-1} peak attributed to an intermediate H-bonding or an incomplete tetrahedral coordination (green) and the ~3600cm^{-1} peak attributed to non H-bonded or free OH stretching (blue). Both of the latter two peaks are attributed to water molecules close to a hydrophobic surface. Values of the absorbance ratio A_{3400}/A_{3200} (intensity of a surface water peak to intensity of the bulk water peak) for films with thicknesses in the range 50÷250nm are within a few percent, in the range 2.05÷2.12.
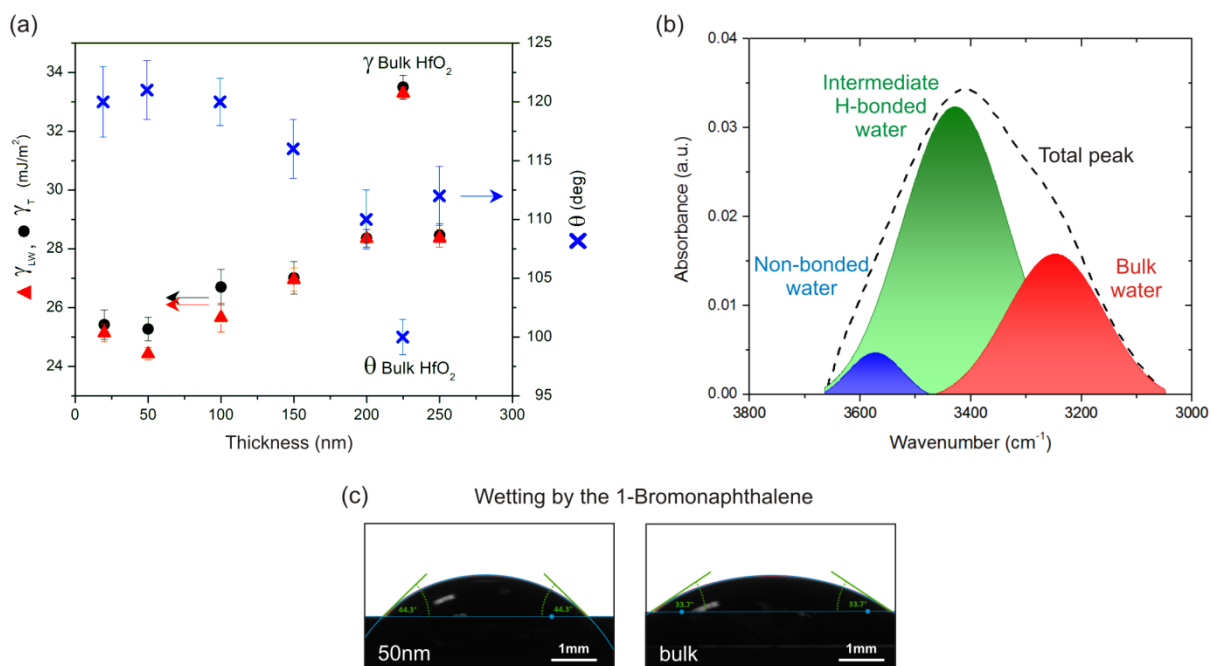

Fig.5.3 a) Dependence of WDCA θ, total surface free energy γ$_T$ and van der Waals component of surface free energy γ$_{LW}$ on the thickness of the HfO$_2$ film , b) FTIR spectrum and its decomposition for water placed on the surface of a 100nm thick HfO$_2$ film, (c) Contact angles of 1-bromonaphthalene for a 50nm-thick film and bulk HfO$_2$

It means that wetting properties are qualitatively the same for all the HfO$_2$ films of different thicknesses with only quantitative differences given by the different values of the surface free energy.

With a decreasing film thickness, the Raman signal in the interval 2800-3000 cm^{-1} containing C-H modes [31] decreased showing that hydrocarbons are not responsible for the increasing hydrophobicity. The film thickness dependence of the wetting properties is also confirmed by the wetting of 1-bromonaphtalene, Fig. 5.3c. In that case the increase of the total surface free energy from $\gamma_{50} \approx 25mJ/m^2$ for the 50nm thick film to $\gamma_{bulk} \approx 33mJ/m^2$ for the bulk HfO$_2$ corresponds to the decrease of the droplet contact angle from $\theta_{50} \approx 43.5°$ to $\theta_{bulk} \approx 34°$.

5.4 Discussion

Thickness dependent wetting behavior of thin films of van der Waals solids like graphene or molybdenum disulfide is observed on the scale of a few atomic layers since the van der Waals surface free energy is given by an integral divergent in its lower limit, and the value of the lower

limit is set by the shortest distance between the liquid molecules and the surface comparable to the lattice constants [12]. Due to the fact that thicknesses of our HfO_2 films are on the order of hundreds of atomic layers, we suggest there is a different mechanism of surface energy dependence. Specifically, two possible explanations are:

1) Influence of the non-dominant texture. An increase of the HfO_2 film thickness is accompanied by an increase of the intensity of the non-dominant (0 0 2) texture of the monoclinic phase. Previous results of calculations of optimized geometries for water molecules adsorbed on the Al-doped ZnO surfaces show different distances between water molecules and the solid with different crystal orientations [32]. Also, there is both experimental [33] and theoretical [34] evidence for the dependence of surface free energy on the crystal orientation in TiN. Therefore growth of the fraction of the (0 0 2) texture intensity to the preferred orientation (-1 1 1) intensity might lead to increasing of the total surface free energy with an increasing film thickness.

2) Changing of the particle size in the material. Surface stress and surface free energy have been reported as decreasing [35, 36], increasing [37] or non-monotonically changing [14] with a decreasing particle size of the material. SEM images of our HfO_2 films show particle sizes in the range of 30÷50nm for the 50÷250nm thick films. In this range of particle sizes, the observed thickness dependence of the surface free energy might therefore indicate a decreasing surface free energy with a decreasing particle size. Yet it is possible that for particle size decreasing further below 30nm, the surface free energy will start increasing again.

Both effects might be acting in parallel both decreasing the surface free energy and thus increasing the contact angle for a decreasing film thickness from 250nm down to 50nm. At a further decrease of the film thickness the two effects might act against each other, so a surface free energy increase due to a decreasing particle size might be compensated by its decrease due to a smaller influence of the non-dominant texture leading to an approximately constant value of 25mJ/m^2 and a consequent approximately constant value of WDCA around 120º.

5.5 Role of the surface contaminants

Recently, the role of the surface contaminants, especially hydrocarbons, on the wetting properties of the various materials was discussed in the literature [25, 39]. Authors explain the hydrophobic effect of the graphene or rare earth oxides by their ability to adsorb the hydrocarbon impurities on the surface. Several methods were declared suitable for cleaning: ultraviolet etching, heating in vacuum or at the atmospheric pressure, ion bombardment and other. In our experiment we compare the contact angle for an as-deposited HfO_2 film with contact angle for films cleaned by:

1) Ion bombardment;
2) Ultrasonically cleaned in acetone;
3) Ultrasonically cleaned in sequence in acetone and in deionised water;

AFM measurements with corresponding contact angles and roughness are given in Fig.5.4
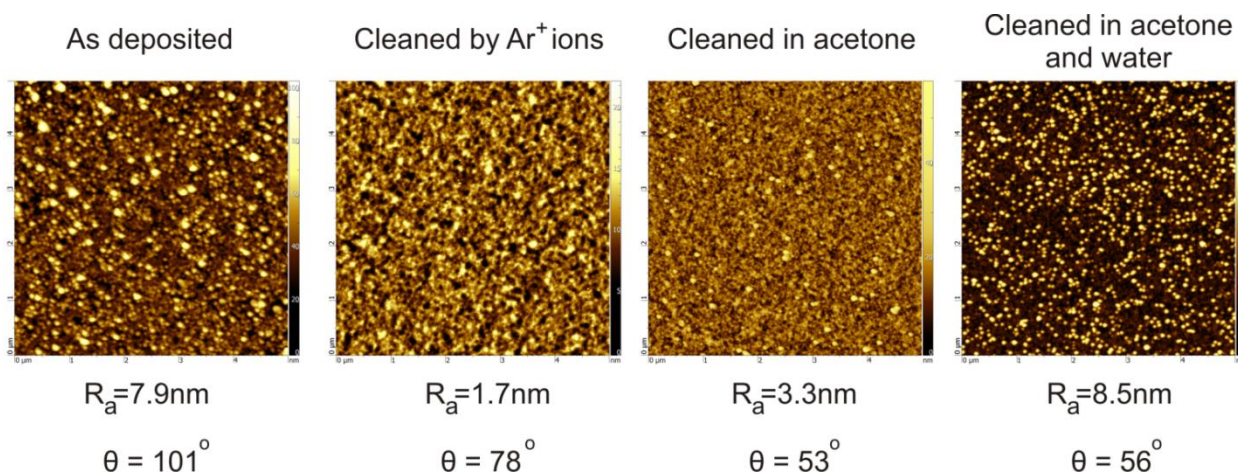
Fig.5.4 Effect of the substrate cleaning by the different techniques in comparison with as deposited films

As can be seen, the results of cleaning by the different methods cannot be used to proove the fact that amount of surface contaminants play the key role in hydrophobicity of HfO_2 films due to the fact that there is no correlation between the contact angle and the purity of the surface. The argon ions etched film show a lower contact angle than the as-deposited film, but at the same time a higher angle in comparison with more "dirty" acetone cleaned surfaces. Heat treatment of various rare-earth oxides also gives non correlated results, since some materials keep their hydrophobic properties, while others start to be hydrophilic [10].

Fig.5.5 Raman spectra for various HfO_2 films: a) as deposited 500nm thick film №1; b) as deposited 500nm thick film №2; c) Ar^+ion etched 500nm thick film; d) as deposited 50nm thick film.

In addition, we have used Raman measurements in order to proove, that adsorption of hydrocarbons is not the key in hydrophobicity of HfO_2 films. Fig.5.5 shows the Raman spectra for selected films.

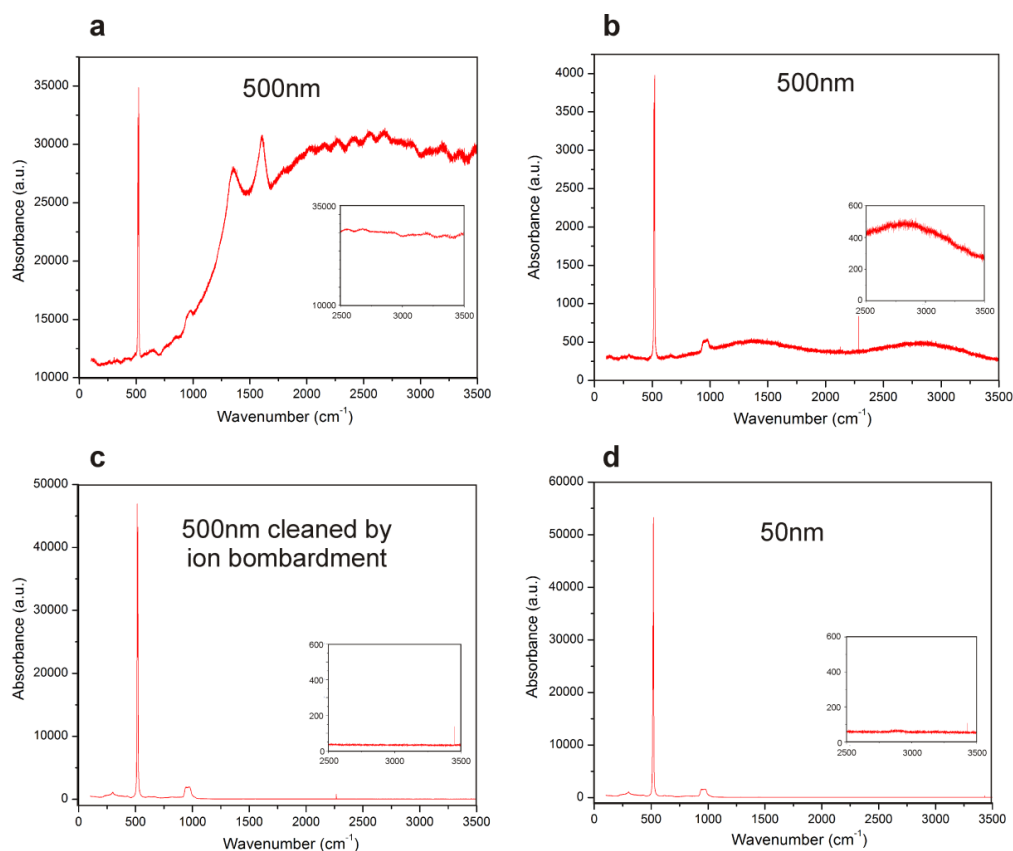Fig.5.5a-b show the Raman spectra for films with the same thickness 500nm and the same contact angle ~100º. The Raman signal in the interval 2800-3000 cm^{-1} containing C-H modes shows completely different amounts of hydrocarbon contamination. At the same time, Fig.5.5c-d represents Ar^+ ion-etched 500nm thick film and as-deposited 50nm thick film, respectively. These films show completely different contact angles, 78º and 120º with comparable Raman spectra, especially in the range of 2800-3000 cm^{-1}, where hydrocarbon stretching frequencies occurs.

All these results, in addition to the measurements in works [10, 24], show that hydrocarbon adsorption does not play the key role in hydrophobicity of compounds of low-electronegativity metals.

5.6 Conclusions

Thickness dependent wetting properties were measured for the intrinsically hydrophobic HfO_2 thin films prepared by reactive high power impulse magnetron sputtering. The van Oss - Good - Chaudhury approach used shows that surface free energy of HfO_2 is $\approx$ 99% electrostatic in nature for all thicknesses. This dominance of the electrostatic Lifshitz − van der Waals component of the surface energy allows to control the value of the contact angle with water in the range 100º÷120º by the variation of the film thickness in the range 50÷250nm. FTIR-ATR measurements show that the wetting properties are qualitatively the same for all HfO_2 films of different thicknesses. Combining these results with XRD and SEM measurements we suggest two mechanisms of surface energy thickness dependence: influence of non-dominant texture and/or non-monotonic size dependence of the particle surface energy. Surfaces with controlled wettability might find various applications such as substrates for controlled morphology of spin-coated films [38].

5.7 References

[1] Preston D. J., Mafra D. L., Miljkovic N., Kong J., Wang E.N. Nano Letters 15, 2015, 2902.

[2] Chen C., Cai Q., Tsai C., Chen C., Xiong G., Yu Y., Ren Z. Applied Physics Letters 90, 2007, 173108.

[3] Kim P., Wong T., Alvarenga J., Kreder M. J., Adorno-Martinez W. E., Aizenberg J. ACS Nano 6, 2012, 6569.

[4] Que´re´, D. Annual Review of Materials Research 38, 2008, 71.

[5] Lu Y., Sathasivam S., Song J., Crick C.R., Carmalt C. J., Parkin I. P. Science 347, 2015, 1132.

[6] Azimi G., Dhiman R., Kwon H., Paxson A. T., Varanasi K. K. Nature Materials 12, 2013, 315.

[7] Zenkin, S., Kos, Š., Musil, J. Journal of the American Ceramic Society 97, 2014, 2713.

[8] Jain R. K., Gautam Y. K., Dave V., Chawla A. K., Chandra R. Applied Surface Science 283, 2013, 332.

[9] Lin S., Liao C. Applied Surface Science (2016), in press

[10] Oh I., Kim K., Lee Z., Ko K. Y., Lee C., Lee S. J., Myung J. M., Lansalot-Matras C., Noh W., Dussarrat C., Kim H., Lee H. Chemistry of Materials 27, 2015, 148.

[11] Rafiee J., Mi X., Gullapalli H., Thomas A. V., Yavari F., Shi Y., Ajayan P. M, Koratkar N. A. Nature Materials 11, 2012, 217.

[12] Shih C., Wang Q. H., Lin S., Park K., Jin Z., Strano M. S., Blankschtein D. Physical Review Letters 109, 2012, 176101.

[13] Gaur A. P. S., Sahoo S., Ahmadi M., Dash S. P., Guinel M .J. -F, Katiyar R. S. Nano Letters 14, 2014, 4314.

[14] Zhang H., Chen B., Banfield J. F. Physical Chemistry Chemical Physics 11, 2009, 2553.

[15] Robertson J. Reports on Progress in Physics 69, 2006, 327.

[16] Gudmundsson J. T., Brenning N., Lundin D., Helmersson U. Journal of Vacuum Science & Technology A 30, 2012, 030801.

[17] Sarakinos K., Alami J., Konstantinidis S. Surface and Coatings Technology 204, 2010, 1661.

[18] Vlček J., Rezek J., Houška J., Kozák T., Kohout J. Vacuum 114, 2015, 131.

[19] Kozák T., Vlček J. Journal of Physics D: Applied Physics 49, 2016, 055202.

[20] Kudláček P., Vlček J., Burcalová K., Lukáš J. Plasma Sources Science and Technology 17, 2008, 025010.

[21] Vlček J., Belosludtsev A., Rezek J., Houška J., Čapek J., Čerstvý R., Haviar S. Surface and Coatings Technology 290, 2016, 58.

[22] Ganesan R., Murdoch B. J., Treverrow B., Ross A. E., Falconer I. S., Kondyurin A., McCulloch D. G., Partridge J.G., McKenzie D. R., Bilek M. M. M. Plasma Sources Science and Technology 24, 2015, 035015.

[23] Sarakinos K., Music D., Mráz S., to Baben M., Jiang K., Nahif F., Braun A., Zilkens C., Konstantinidis S., Renaux F., Cossement D., Munnik F., Schneider J. M. Journal of Applied Physics 108, 2010, 014904.

[24] Khan S., Azimi G., Yildiz B., Varanasi K. K. Applied Physics Letters 6, 2015, 061601.

[25] Preston D. J., Miljkovic N., Sack J., Enright R., Queeney J., Wang E. N. Applied Physics Letters 105, 2014, 011601.

[26] H. H. Kung, *Transition Metal Oxides: Surface Chemistry and Catalysis*; Elsevier, Netherlands, 1989.

[27] International Centre for Diffraction Data, PDF-2 Database Sets 1-47, 1997. (Pennsylvania, U.S.A.).

[28] van Oss C. J., Good R. J., Chaudhury M. K. Langmuir 4, 1988, 884.

[29] Yalamanchili M. R., Atia A. A., Miller J. D. Langmuir 12, 1996, 4176.

[30] Scatena L. F., Brown M. G., Richmond G. L. Science 292, 2001, 908.

[31] Li Z., Wang Y., Kozbial A., Shenoy G., Zhou F., McGinley R., Ireland P., Morganstein B., Kunkel A., Surwade S. P., Li L., Liu H., Nature Materials 12, 2013, 925.

[32] Wang J., Li Y., Kong Y., Zhou J., Wu J., Wu X., Qin W., Jiao Z., Jiang L. RSC Advances 5, 2015, 81024.

[33] Oh U.C., Je J.H., Journal of Applied Physics 74, 1993, 1692.

[34] Marlo M., Milman V., Physical Review B 62 , 2000, 2899.

[35] Ouyang G., 10 Tan X., Yang G. Physical Review B 74, 2006, 195408.

[36] Jiang Q., Zhao D. S., Zhao M. Acta Materialia 49, 2001, 3143.

[37] Muller E.,Vogelsberger W., Fritsche H.-G. Crystal Research and Technology 23, 1988, 1153.

[38] Bi C., Wang Q., Shao Y., Yuan Y., Xiao Z., Huang J., Nature Communications 6, 2015, 7747.

[39] Z. Li et al. Nature Materials 12, 2013, 925.

CHAPTER 6

PHYSICAL AND MECHANICAL PROPERTIES OF CRYSTALLINE AND NANOCRYSTALLINE Zr-Ti ALLOY PREPARED BY DC MAGNETRON SPUTTERING

6.1. Introduction

In recent years, binary zirconium-titanium alloys have been an object of the intensive research stimulated by their good mechanical properties such as high hardness, high strength-to-weight ratio, and high fracture toughness [1-3], enhanced corrosion resistance [4,5] and excellent biocompabillity [4,6-11]. According to the phase diagram the ZrTi alloy creates only the solid solution for any composition of alloy due to almost zero heat of mixing [7]; $\Delta H_{ZrTi} = 0$ for 50 at.% Zr and 50 at.% Ti [8]. Metallurgical processes such as melting and casting create the alloys with a macro sized crystal structure [8]. On the other hand, widely used PVD processes allow form the nanocrystalline and amorphous alloy films [7].

The nanocrystalline alloy films can be easily formed if they are produced under a strong ion bombardment of the growing film, for example, using ion plating sputtering process. This process is based on the grain refinement by stopping of the grain growth during ion bombardment. The nanocrystallization process can be further enhanced in the case when (i) a small amount of one of the metal elements (Me_1 or Me_2) in the (Me_1,Me_2) alloy is replaced by a small addition of the reactive gas atoms (O, N, C, etc.), i.e. (Me_1,Me_2,O) alloy film is formed or (ii) the metalloid atoms (As, Te, Ge, Si, Sb, B) replace one of the metal element (Me_1 or Me_2), i.e. (Me_1,Met) alloy film is formed [12]; here Met is the metalloid atom. In the (Me_1,Me_2) alloy film there are weak metallic bonds between the metal atoms (approx. 1.46 eV for Ti-Ti atoms [13]) and the high mobility of atoms on the surface of growing film what results in the growth of well-developed crystalline grains. On the contrary, the oxide and nitride films have strong metal-oxygen and metal-nitrogen bonds (6.86 eV and 4.81 eV for Ti-O and Ti-N, respectively [13] and thereby the atoms forming molecules exhibit a low mobility on the surface of growing film. Strong covalent or ionic bonds in materials of such films slow down the motion of individual atoms on their surfaces during growth and thereby prevent atoms to reach positions necessary to form the crystalline film. Therefore, the (Me_1,Me_2) alloy films with added reactive gas atoms, i.e. (Me_1,Me_2,O) or (Me_1,Me_2,N) alloy films with a small addition of O or N, deposited on the unheated substrate can exhibit strongly nanocrystalline structure. The same effect, i.e. the film nanocrystallization, can be achieved in the case of the (Me,Met) alloy films. In the case when the ratio of Met and Me atoms (Met/Me) is correctly selected the (Me,Met) alloy film can exhibit even fully disordered (X-ray amorphous) structure, for instance, the $a - (Al,Ti)$ alloy films in the $Al - Ti$ and Al-Si alloy systems can be formed [12].

This article shows how (1) the structure of the (Me_1,Me_2) alloy film varies from crystalline to nanocrystalline under ion bombardment and (2) the nanocrystallization of the (Me_1,Me_2) alloy film can be enhanced in the case when a small amount of oxygen is incorporated in the (Me_1,Me_2) alloy, i.e. when the (Me_1,Me_2,O) alloy film is formed. To demonstrate the effect of the ion bombardment on the structure of the (Me_1/Me_2) alloy film and the enhancement of the nanocrystallization in the (Me_1,Me_2,O) alloy film the (Zr,Ti) and (Zr,Ti,O) alloy films with three elemental compositions − $Zr_{95}Ti_5$, $Zr_{30}Ti_{70}$ and Zr_5Ti_{95} were selected. The main aim of this article is to show under which conditions it is possible to sputter the flexible alloy based films with enhanced hardness H and resistance to cracking.

6.2 Experimental details

The Zr-Ti alloy films were sputtered using a round unbalanced magnetron equipped with a Zr target of diameter 100 mm fixed to the magnetron by Ti ring with three inner diameters $\varnothing_I = 70$, 40 and 30 mm. This target enables to sputter the Zr-Ti alloy films with three elemental compositions: the $Zr_{95}Ti_5$, $Zr_{30}Ti_{70}$ and Zr_5Ti_{95} films, respectively. The magnetron was supplied by a DC power supply (1 kV, 5A). The films were sputtered on Si (100) substrates (20 x 20 x 0.525 mm^3 and 35 x 5 x 0.525 mm^3) and a Mo strip (50 x 15 x 0.1 mm^3) under the following deposition conditions: discharge current $I_d = 1$ A, substrate temperature $T_s = 450°C$, substrate bias $U_s = -50, -100, -150, -200,$ and $-250V$, substrate–to-target distance $d_{s-t} = 60$ mm and argon pressure $p_{Ar} = 1$ Pa. The film thickness h and the surface roughness R_a were determined using the electro-mechanical stylus profilometer (Dektak 8 Stylus Profiler, VEECO, Plainview, NY). The structure of films was characterized by X-ray diffraction (XRD) using a diffractometer (X'Pert PRO; PANanalytical, ALMELLO, the Netherlands). The hardness H, effective Young's modulus E^* and elastic recovery W_e of films were determined from load versus displacement curves measured by a computer controlled microhardness tester (Fischerscope H100 VP XY PROG, Windsor, CT) equipped with a Vicker's diamond indenter at load L = 20 mN. The resistance of films to cracking was characterized by (i) the bending test (the Mo strip coated with the sputtered film was bent around a fixed cylinder of radius r = 5 mm) and (ii) the indentation test at a high diamond indenter load L (the impression of the diamond indenter in the surface of film at high load L = 0.2 N); more details are given in Ref. [14]. The surface morphology of (i) the films with impressions of the diamond indenter and (ii) the bent films deposited on the Mo strips was investigated by an optical microscope. The fracture cross-sections of the films deposited on Si (100) substrate were investigated by a Hitachi SU-70 scanning electron microscope (SEM).

6.3 Results and discussion

6.3.1 Structure

The structure of the sputtered Zr-Ti alloy film strongly depends on its elemental composition and the energy E_{bi} delivered to the growing film by bombarding ions, see Fig. 6.1. The energy E_{bi} is controlled by the negative substrate bias U_s. The energy E_{bi} can be assessed from the formula $E_{bi} = U_s i_s / a_D$ [15]; here i_s is the substrate ion current density and a_D is the film deposition rate a_D. The relationships between E_{bi} and deposition parameters are given in Table 6.1. The film structure is characterized by XRD patterns. Fig.6.1 displays the evolution of the structure of Zr-Ti alloy with increasing negative substrate bias U_s for three elemental compositions: $Zr_{95}Ti_5$, $Zr_{30}Ti_{70}$ and Zr_5Ti_{95}. From this experiment four important issues can be drawn:

(1) All sputtered Zr-Ti films are solid solution films as predicts the binary phase diagram of Zr-Ti [16].

(2) The Zr-Ti films with small amount of Ti (≤ 5 at.%) are the alloy films with the α-Zr phase. On the other hand, the Zr-Ti films with high amount of Ti (≥ 70 at.%) are the alloy films with the α-Ti phase.

(3) The Zr-Ti alloy films are well crystalline and exhibit a strong texture, α-Zr(002) for $Zr_{95}Ti_5$ film and α-Ti(002) for $Zr_{30}Ti_{70}$ and Zr_5Ti_{95} films, when they are sputtered at the low negative bias $U_s = -50$ V.

(4) The Zr-Ti alloy films sputtered at high negative biases $|U_s| \geq 150$ V, i.e. at a high ion bombardment, are nanocrystalline as very low and broad intensities of the reflection peaks indicate.
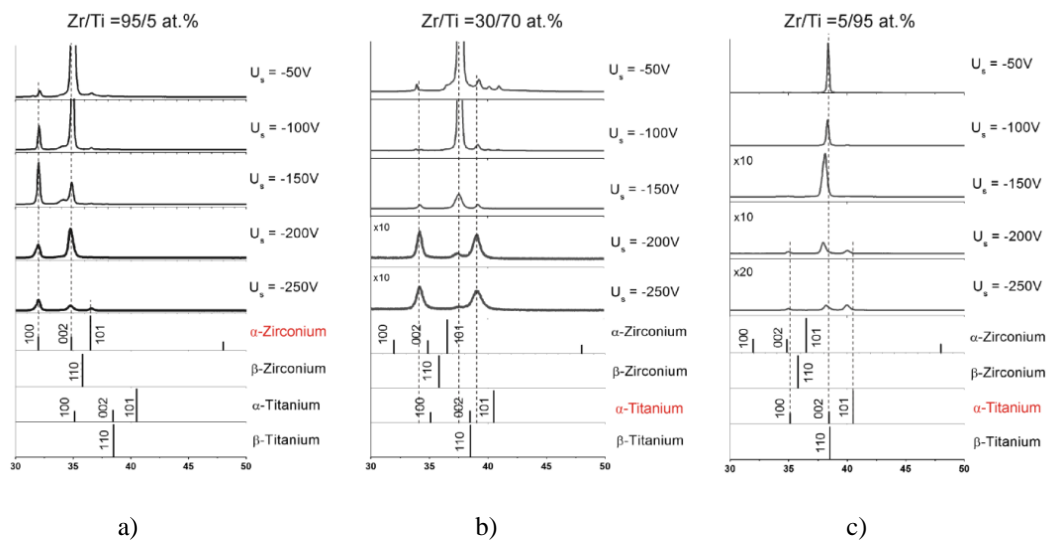

a)   b)   c)

Fig.6.1 XRD patterns of the ZrTi films with (a) 5 at.% Ti, (b) 70 at.% Ti and (c) 95 at.% Ti, sputtered at $I_d = 1$ A, $U_d = 350$ V, $T_s = 450\,°C$, $d_{s-t} = 60$ mm, $p_{Ar} = 1$ Pa and five values of the substrate bias $U_s = -50, -100, -150, -200,$ and $-250V$.

Table 6.1 Relationships between the energy E_{bi} and the deposition parameters of the Zr-Ti alloy films with three elemental compositions.

	$Zr_{95}Ti_5$				$Zr_{30}Ti_{70}$				Zr_5Ti_{95}			
U_s [V]	h [nm]	i_s [ma/cm^2]	a_D [nm/min]	E_{bi} [MJ/cm^3]	h [nm]	i_s [ma/cm^2]	a_D [nm/min]	E_{bi} [MJ/cm^3]	h [nm]	i_s [ma/cm^2]	a_D [nm/min]	E_{bi} [MJ/cm^3]
-50	1760	0.73	89	0.247	3400	0.98	57	0.52	3120	1.34	52	0.77
-100	1850	1.27	93	0.823	3050	1.59	50	1.91	2870	1.85	48	2.32
-150	1700	1.59	85	1.683	3000	1.84	51	3.25	3000	2.10	50	3.64
-200	1630	1.91	81	2.826	3100	2.04	52	4.47	2580	2.23	43	5.51
-250	1850	1.97	76	3.909	3120	2.23	52	6.43	2400	2.30	40	8.60

From Fig.6.1 and Table 6.1 it is seen that the nanocrystalline Zr-Ti alloy films are formed when the energy delivered by bombarding ions $E_{bi} \geq 3.5$ MJ/cm^3 independently on the elemental composition of the alloy material. This finding can be of great importance for many practical applications.

6.3.2 Mechanical properties

Mechanical properties of the sputtered Zr-Ti alloy films are summarized in Fig.6.2 and Table 6.2. Fig.6.2 displays the evolution of the hardness H and the effective Young's modulus E^* with increasing energy E_{bi}. From this figure it is seen that (1) the values of H and E^* are approximately constant for $E_{bi} < 4$ MJ/cm^3 and slightly decrease with $E_{bi} \geq 4$ MJ/cm^3 what is

connected with the conversion of the crystalline Zr-Ti films to nanocrystalline ones and (2) the hardness H decreases with increasing content of Ti in the alloy (H ≈ 6 GPa for $Zr_{95}Ti_5$ film and H ≈ 4 GPa for Zr_9Ti_{95} film). The Table 6.2 shows that all sputtered Zr-Ti films exhibit the low values of (i) the ratio $H/E^* < 0.1$, (ii) the elastic recovery $W_e < 35\%$ and (iii) the macrostress $\sigma < 1$ GPa. It indicates that the sputtered Zr-Ti alloy films are brittle; for more details see Ref. [17]
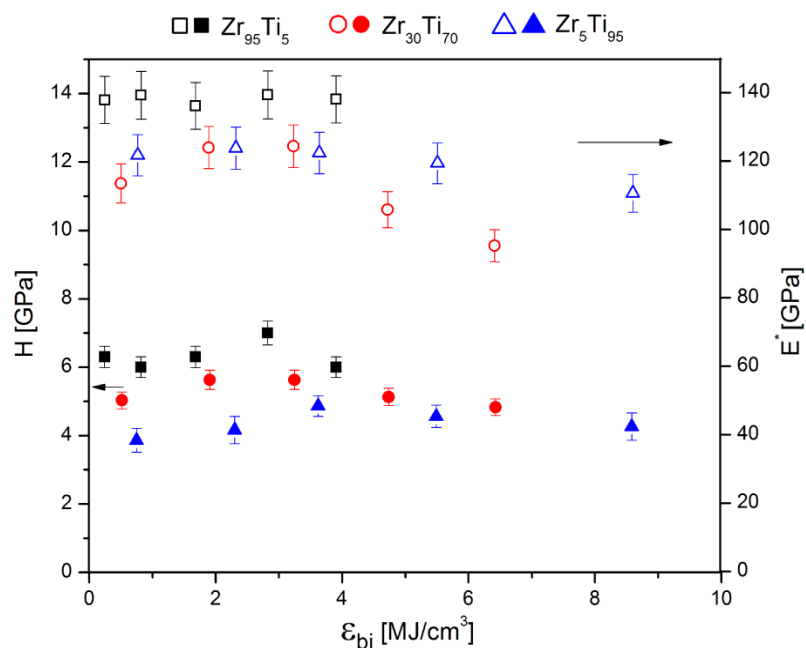

Fig.6.2. Hardness H and effective Young's modulus E^* of the ZrTi films with 5 at.% Ti (squares), 70 at.% Ti (circles) and 95 at.% Ti (triangles), sputtered at $I_d = 1$ A, $U_d = 350$ V, $T_s = 450$ °C, $d_{s-t} = 60$ mm, $p_{Ar} = 1$ Pa as a function of energy E_{bi}.

Table 6.2. Relationships between the energy E_{bi} and the mechanical properties of the Zr-Ti alloy films with three elemental compositions.

$Zr_{95}Ti_5$					$Zr_{30}Ti_{70}$					Zr_5Ti_{95}				
E_{bi} [MJ/cm^3]	H [GPa]	H/E^*	W_e [%]	σ [GPa]	E_{bi} [MJ/cm^3]	H [GPa]	H/E^*	W_e [%]	σ [GPa]	E_{bi} [MJ/cm^3]	H [GPa]	H/E^*	W_e [%]	σ [GPa]
0.247	6.3	0.046	32	0.3	0.52	5.1	0.043	28	0.5	0.77	3.8	0.031	22	0.2
0.823	6.0	0.043	30	-0.2	1.91	5.0	0.044	31	0.3	2.32	4.1	0.033	24	0
1.683	6.3	0.043	33	-0.9	3.25	5.6	0.045	30	-0.2	3.64	4.8	0.039	28	-0.2
2.826	7.0	0.050	35	-0.7	4.74	5.6	0.045	31	-0.3	5.51	4.5	0.038	27	-0.3
3.909	5.9	0.041	31	-0.8	6.43	4.5	0.047	33	-0.3	8.60	4.2	0.038	26	-0.3

6.3.3 Effect of substrate temperature and energy of bombarding ions on the structure of Zr-Ti films

The substrate temperature T_s seems to have a similar effect on the structure of sputtered Zr-Ti alloy film as the energy E_{bi} delivered by bombarding ions. The structure of the $Zr_{30}Ti_{70}$ alloy film sputtered at T_s = RT (unheated substrate) and T_s =450°C and the same substrate bias U_s = -200 V is displayed in Fig.6.3. This figure shows that while the $Zr_{30}Ti_{70}$ alloy film sputtered on the unheated substrate (T_s = RT) is well crystalline, the $Zr_{30}Ti_{70}$ alloy film sputtered on the heated substrate (T_s = 450°C) is nanocrystalline. This great difference in the film structure is not, however, due to different substrate temperatures T_s but it is due to different values of the energy E_{bi} caused by different deposition rates a_D of films sputtered with the new (non-sputtered) target used at T_s = RT (higher target power density W_t = I_dU_d due to a higher U_d at I_d = 1 A, higher deposition rate a_D = 75 nm/min, and thus lower energy E_{bi} = 3.2 MJ/cm^3) and the old (strongly used) target at T_s = 450°C (lower W_t due to lower U_d at I_d = 1 A, lower a_D = 51 nm/min and thus higher E_{bi} = 4.74 MJ/cm^3). This experiment shows that the knowledge of the energy E_{bi} is very important because it makes possible to find the correct cause responsible for nanocrystallization process. In our experiment a huge change in T_s from RT to 450°C is not responsible for the conversion of the crystalline film to nanocrystalline but the increase of E_{bi} what results in the nanocrystallization induced by stronger ion bombardment at the same substrate bias U_s = -200 V.
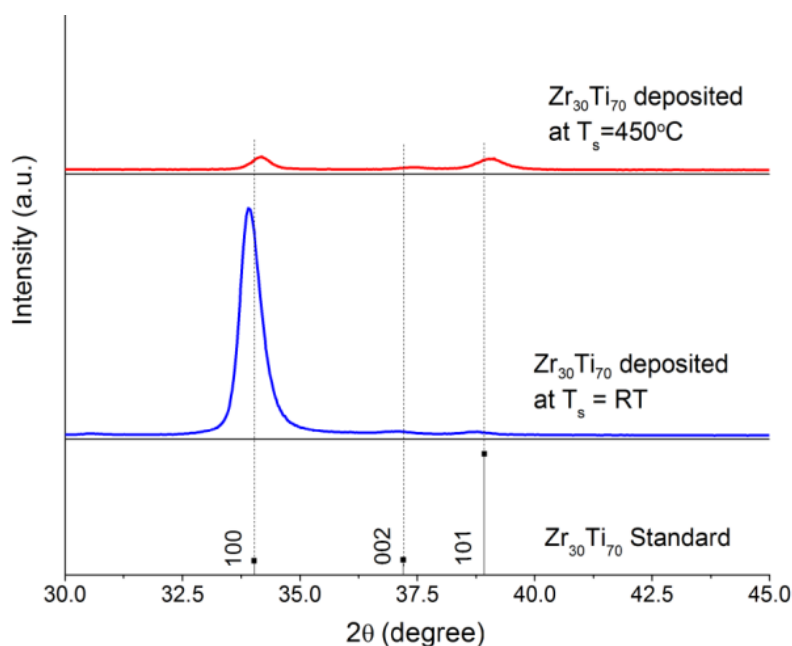

Fig.6.3. XRD patterns of as-deposited $Zr_{30}Ti_{70}$ film sputtered on Si (100) substrate at I_d = 1 A, U_s = -200 V, p_{Ar} = 1 Pa and two values of substrate temperature T_s = RT (unheated substrate) and T_s = 450 °C.

6.3.4 Nanocrystalization of Zr-Ti alloy films induced by addition of oxygen

The nanocrystallization of the Zr-Ti alloy film can be controlled not only by the energy E_{bi} as shown above but also by the addition of a small amount of oxygen in the sputtered alloy film. This possibility was demonstrated in sputtering of the $Zr_{30}Ti_{70}$ alloy films in (i) the pure argon and (ii) the argon mixed with a very small amount of oxygen at pressure p = 1 Pa, constant flow

rate of argon ϕ_{Ar} = 32.5 sccm and three values of flow rate of oxygen ϕ_{O2} = 1, 1.5 and 2 sccm. The sputtered films were characterized by a X-ray diffraction and obtained results are given in Fig.6.4 and in Table 6.3. Sputtered films are characterized by the α-Ti (100) reflection whose intensity strongly decreases with increasing addition of O_2 into argon sputtering gas. Already at very small addition of O_2 (ϕ_{O2} = 2 sccm) a nanocrystalline $Zr_{30}Ti_{70}O_x$ alloy film is formed.
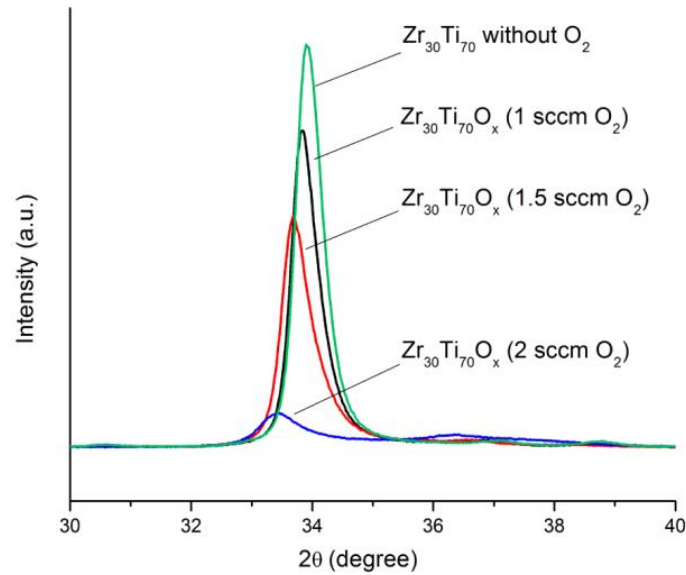

Fig.6.4. XRD patterns of as-deposited $Zr_{30}Ti_{70}O_x$ film sputtered on unheated Si (100) substrate (T_s = RT) in Ar + O_2 sputtering gas at total pressure $p_T = p_{Ar} + p_{O2} \approx 1$ Pa, constant flow rate of argon ϕ_{Ar} =32.5 sccm and three values of flow rate of oxygen ϕ_{o2} = 1.0, 1.5 and 2.0 sccm.

This film exhibits also strong enhancement of its hardness H up to 16 GPa, H/E^* ratio above 0.1 and elastic recovery W_e above 60% what are conditions necessary for the creation of film with enhanced resistance to cracking [17]. The enhanced resistance of the nanocrystalline (Zr,Ti,O) alloy film to cracking was experimentally confirmed, see the section 6.3.6. In summary, it can be concluded that a very small addition of O_2 into argon sputtering gas induces the nanocrystallization of sputtered (Zr,Ti,O) alloy film and strongly enhances its resistance to cracking, see Table 6.3.

Table 6.3 Mechanical properties and macrostress σ of 1150 nm thick $Zr_{30}Ti_{70}$ alloy sputtered at I_d = 1 A, U_s = -200V, T_s = RT (unheated substrate), i_s = 2 mA/cm², E_{bi} = 3.2 MJ/cm³, p = 1 Pa with deposition rate a_D = 75 nm/min in pure argon and argon mixed with a very small amount of oxygen

O_2 [sccm]	H [GPa]	E^* [GPa]	H/E^*	W_e [%]	σ [GPa]
0	5	115	0.043	33	-0.3
1	8.6	130	0.066	44	-0.8
1.5	10.5	133	0.079	50	-0.8
2	16	152	0.15	63	-0.9

6.3.5 Microstructure of (Zr,Ti,O) alloy films

The cross-section microstructure of the $Zr_{30}Ti_{70}$ alloy films sputtered in argon mixed with a very small amount of oxygen (ϕ_{Ar} = 32.5 sccm + ϕ_{O2} = 1, 1.5 or 2 sccm, respectively) are displayed in Fig.6.5. From this figure it is seen that while the (Zr,Ti,O) alloy films sputtered at ϕ_{O2} < 2 sccm exhibit a columnar-like microstructure, the (Zr,Ti,O) film sputtered at ϕ_{O2} = 2 sccm exhibits dense, voids-free, non-columnar microstructure. The change of the microstructure of the film sputtered at ϕ_{O2} = 2 sccm correlates well with (i) the conversion of the crystalline films to the nanocrystalline one and (ii) the strong increase of its H, H/E* ratio, W_e.
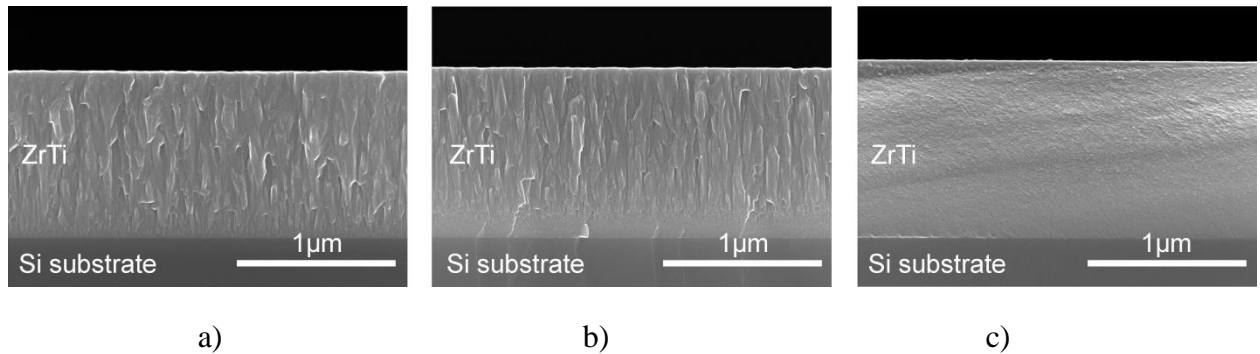

a)   b)   c)

Fig.6.5 SEM images of cross-section of as-deposited $Zr_{30}Ti_{70}O_x$ films sputtered on unheated Si (100) substrate (T_s = RT) in Ar with small addition of oxygen at total pressure $p_T = p_{Ar} + p_{O2} \approx 1$ Pa, constant flow rate of argon ϕ_{Ar} =32.5 sccm and three values of flow rate of oxygen (a) ϕ_{02} = 1 sccm, (b) ϕ_{02} = 1.5 sccm and (c) ϕ_{02} = 2 sccm.

6.3.6 Resistance of (Zr,Ti,O) alloy film to cracking

The resistance of (Zr,Ti,O) alloy films was assessed by (i) the indentation test (Fig.6.6a) and (ii) bending test (Fig.6.6b). In the indentation test the diamond indenter was impressed in the surface of film at a high load L = 0.2 N, in the bending test the Mo strip (50 x 15 x 0.1 mm^3) coated by the (Zr.Ti,O) film was bended around a fixed cylinder of radius r = 5 mm; more details are given in Ref. [14]. Fig.6.6a shows the cracks in the crystalline (Zr.Ti,O) films with columnar-like microstructure sputtered with small addition of O_2 (ϕ_{O2} < 2 sccm). On the other hand, the nanocrystalline (Zr.Ti,O) film with dense, voids-free, non-columnar microstructure sputtered at ϕ_{O2} = 2 sccm does not crack because its higher H, H/E* ratio and W_e compared with the films sputtered at ϕ_{O2} < 2 sccm. In the indentation test the film is loaded perpendicularly to its surface. In the bending test (the loading is along the film surface) no cracks are formed up to the strain ε = h_{Mo}/2r = 0.02, i.e. the strain induced by bending around the fixed cylinder of radius r = 5 mm (the minimal radius used in our tests), see Fig.6.6b; for more details see Ref. [14]. This experiment shows that both the crystalline and nanocrystalline (Zr,Ti,O) alloy films exhibit the enhanced resistance to cracking in bending, i.e. in the tension test. In the compression test, i.e. in the indentation test, the enhanced resistance to cracking exhibit only the (Zr,Ti,O) film with high hardness H = 16 GPa, high ratio H/E* = 0.105, high W_e = 63 % and dense, voids-free non-columnar microstructure sputtered at ϕ_{O2} = 2 sccm.
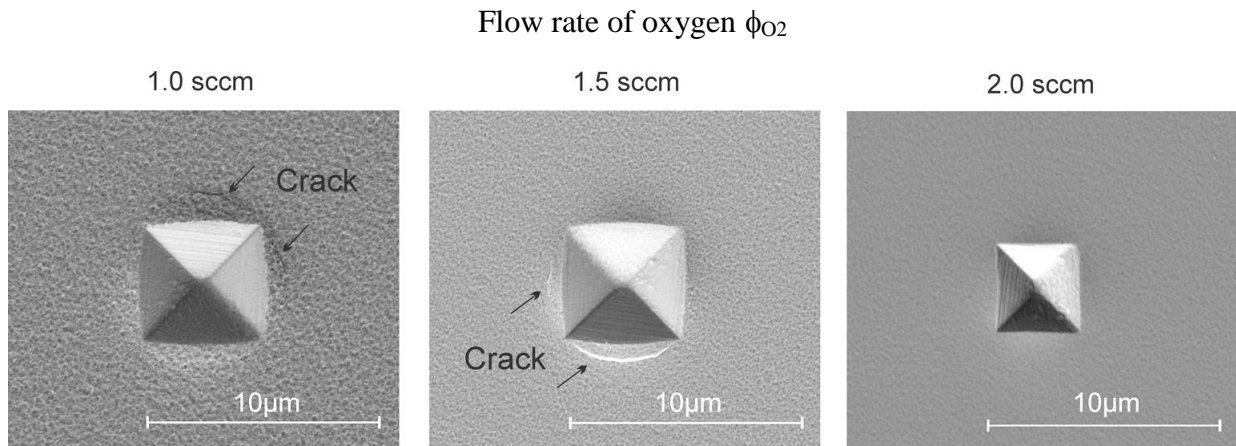
Flow rate of oxygen ϕ_{O2}

Fig.6.6a Surface morphology of (Zr,Ti,O) film deposited on Si (100) substrate after diamond impression at a high load L = 0.2 N. Indentation depth for all three films was d/h = 0.5.
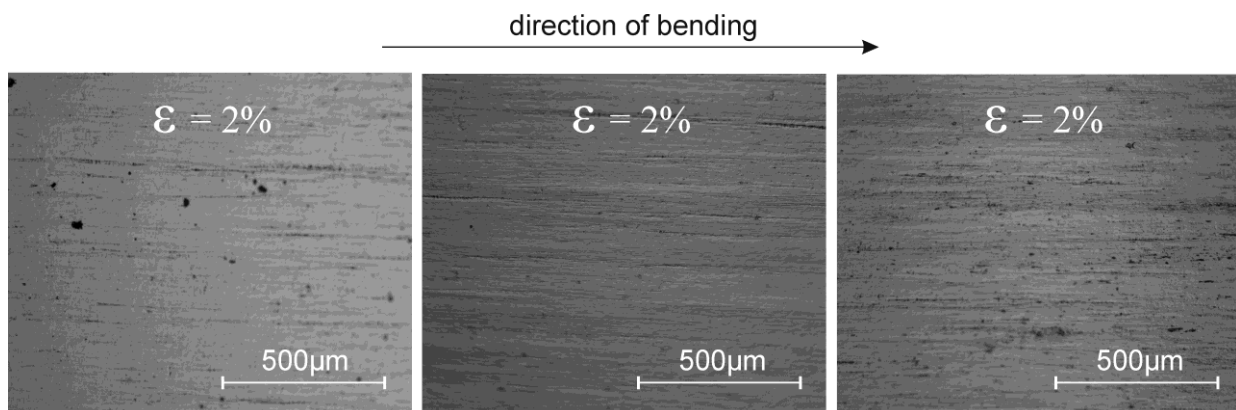
direction of bending

Fig.6.6b Surface morphology of $Zr_{30}Ti_{70}O_x$ film deposited on Mo strip (50 x 15 x 0.1 mm^3) after bending around a fixed cylinder of diameter r = 5 mm.

6.3.7 Strength-to-weight ratio of (Zr,Ti,O) alloy films

The strength-to weight σ_{UTS}/ρ ratio is very important parameter characterizing the quality of the film; here σ_{UTS} is the ultimate tensile strength and ρ is the density of the film material. The ultimate tensile strength σ_{UTS} of the ductile metallic and alloy films can be calculated from the formula H $\approx$ 3σ_{UTS}; here H is the hardness of film [18]. The values of the σ_{UTS}/ρ ratio of the sputtered (Zr,Ti,O) films, calculated from the measured values of their hardness H and density ρ (determined from the measured weight and volume of the film), are displayed in Fig.6.7. In this figure also regions with low and enhanced resistance to cracking of the (Zr,Ti,O) films are given. Besides, the values of the ultimate tensile strength for the Zr-400 alloy, Fe-Co based and Zr-Ti based metallic glasess (MG) and ceramics are also given in Fig.6.7 for a comparison [18]. Fig.6.7 shows that:

1. The ultimate tensile strength of the sputtered (Zr,Ti) film is low of about 1.6 GPa but strongly increases with addition of O in the (Zr,Ti) alloy due to an increase of the hardness H of the (Zr,Ti,O) alloy film.

2. The (Zr,Ti,O) alloy films with $\sigma_{UTS} \geq$ 4 GPa exhibit an enhanced resistance to cracking.

3. The very high ultimate tensile strength $\sigma_{UTS} \approx 5.5$ GPa of (Zr,Ti,O) alloy film is comparable with that of the best Fe-Co based MG reported in Ref. [18] but the density ρ of the (Zr,Ti,O) alloy film is considerably lower and close to the mass density ρ of the Zr-based MG.

The hardness H of the (Zr,Ti) alloy film is low H $\leq$ 6 GPa. The hardness can be, however, increased in the case when a small amount of O is incorporated in the film and a nanocrystalline oxide phase embedded in the (Zr,Ti) alloy matrix is formed. This experiment in which O is incorporated in the alloy indicates that the absence of the second nanocrystalline phase in the alloy is the main reason why the pure alloy films cannot exhibit an enhanced hardness H.
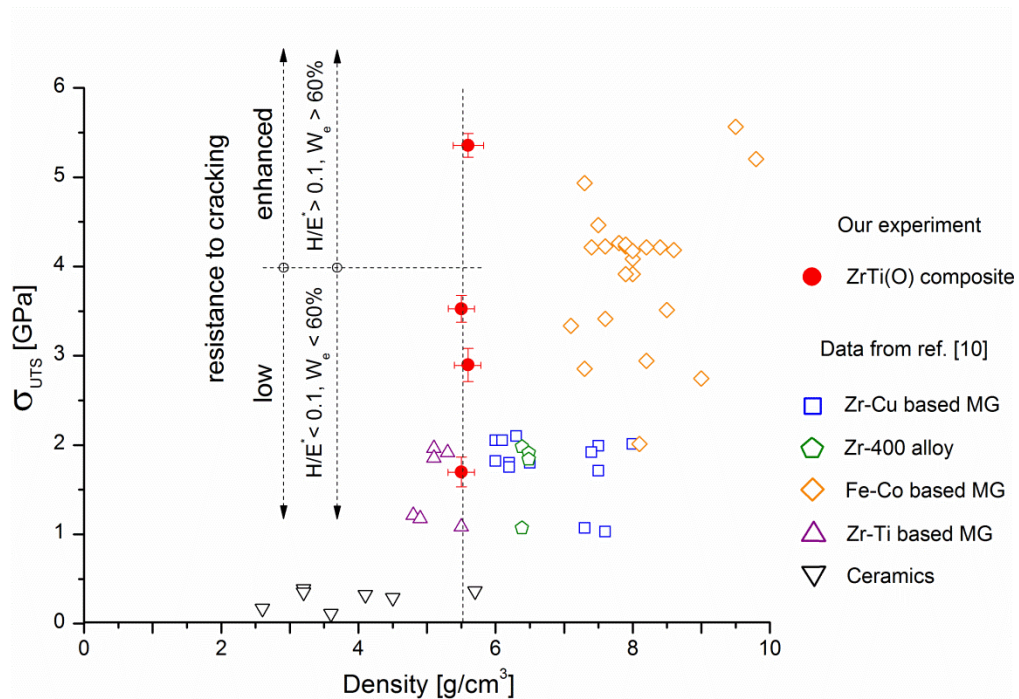

Fig.6.7. The ultimate tensile strength σ_{UTS} of the sputtered (Zr,Ti,O) alloy films as a function of its mass density ρ. The values of σ_{UTS} for the Zr-400 alloy, Fe-Co and Zr-Ti based MG and ceramics reported in Ref. [18] are given for a comparison.

6.4 Conclusions

The main results of the detailed investigation of the structure, microstructure, physical and mechanical properties of sputtered Zr,-Ti alloy films with different elemental composition can be summarized as follows:

1. All sputtered Zr-Ti films are solid solution films as predicts the binary phase diagram of the (Zr,Ti) alloy [16].

2. The (Zr,Ti) alloy films with small amount of Ti ($\leq$ 5 at.%) are the alloy films with the α-Zr phase. On the other hand, the (Zr,Ti) alloy films with high amount of Ti ($\geq$ 70 at.%) are the alloy films with the α-Ti phase.

3. The (Zr,Ti) alloy films are well crystalline and exhibit a strong texture, α-Zr(002) for the $Zr_{95}Ti_5$ film and α-Ti(002) for the $Zr_{30}Ti_{70}$ and Zr_5Ti_{95} films, when are sputtered at low negative bias $U_s = -50$ V.

4. The crystallinity of the (Zr,Ti) alloy films can be strongly reduced by (i) the strong ion bombardment of growing film, i.e. when they are sputtered at high negative substrate biases $|U_s| \geq 150$ V, and (ii) the addition of a small of oxygen in the argon sputtering gas. Both methods allow form the nanocrystalline Zr-Ti alloy films.

5. The (Zr,Ti,O) alloy films with addition of a small amount of O ($\phi_{O2} < 2$ sccm) are brittle and easily crack due to low hardness H < 10 GPa, low ratio $H/E^* < 0.1$ ratio and low elastic recovery $W_e < 60\%$. On the other hand, the (Zr,Ti,O) alloy films with addition of a higher amount of O ($\phi_{O2} \geq 2$ sccm) exhibit an enhanced resistance to cracking because they have the high hardness H = 16 GPa, high ratio $H/E^* \geq 0.1$ and high elastic recovery $W_e \geq 60\%$.

6. The incorporation of a small of O in (Zr,Ti) alloy film is very effective way to increase its hardness H and to form the flexible (Zr,Ti,O) alloy films with enhanced resistance to cracking.

The main result of presented investigation is the finding that a small addition of oxygen in the (Zr,Ti) alloy film makes it possible to create the flexible (Zr,Ti,O) alloy films with high hardness H ≈ 15 GPa and enhanced resistance to cracking.

Acknowledgements

6.5 References

[1] A.L. Greer: Metallic Glasses, Science 267, 1995, 1947.

[2] C. J. Gilbert, R. O. Ritchie and W. L. Johnson, Applied Physics Letters 71, 1997, 476.

[3]D.R.N.Correa, F.B.Vicente, T.A.G.Donato, V.E.Arana-Chavez, M.A.R.Buzalaf, C.R.Grandini, Materials Science and Engineering: C 34, 2014, 354.

[4] M. Long, H.J. Rack Biomaterials 19, 1998, 1621.

[5] W.F.Cui, C.J.Shao, Surface and Coatings Technology 283, 2015, 101.

[6] E. Eisenbarth, D. Velten, M. Müller, R. Thull, J. Breme, Biomaterials 25, 2004, 5705.

[7] C.J. Chen et al. Journal of Alloys and Compounds 483, 2009, 337.

[8] Hsueh-Chuan Hsu et al. Journal of Alloys and Compounds 488, 2009, 279.

[9] H.M.Grandin, S.Berner, M.Dard, Materials 5, 2012, 1348.

[10] C.Picconi, G.Maccauro, Biomaterials 20, 2001, 1

[11] M.T.Tsai, Y.Y.Chang, H.L.Huang, Y.H.Wu, T.M.Shieh, Surface and Coatings Technology 303, 2016, 268

[12] M.Naka, T.Shibayanagi, M.Maeda, S.Zhao, H.Mori, Vacuum 59, 2000, 252.

[13] T.L.Cottrell: *The Strengths of Chemical Bonds*, 2nd Edition, Butterworth, London, 1958.

[14] J.Musil: *Advanced hard coating with enhanced toughness and resistance to cracking, in: S.Zhang(Ed.), Chapter 7 in the Book Thin Films and Coatings. Toughening and Toughness Characterization,* CRC Press, USA, 2015.

[15] J.Musil, J.Šícha, D.Heřman, R.Čerstvý, Journal of Vacuum Science & Technology A 25, 2007, 666.

[16] *Smithells Metals Reference Book*, Eight Edition, *W.F.Gale and T.C.Totemeier (Eds.),* Elsevier 2004.

[17] J.Musil, RSC Advances 5, 2015, 60482.

[18] P.Zhang, S.X.Li, Z.F.Zhang, Materials Science and Engineering A 529, 2011, 62.

7. MAIN CONCLUSIONS

This PhD thesis is dedicated to the preparation and characterization of the multifunctional ceramic and metal thin films with an enhanced resistance to cracking. Also, their wetting properties were characterized and discussed. It is possible to conclude that:

1) Metals with low-electronegativity (Mg, Y, Zr and Hf), similar to the electronegativity of the lanthanide group metals ($\chi \sim 1.1$-1.3), form hydrophobic oxides and nitrides with the water droplet contact angle $\theta > 90°$. Therefore, it is possible to produce hard hydrophobic ceramic surfaces without the use of the rare-earth elements.

2) Nitrides of the low-electronegativity metals show higher water droplet contact angles than the corresponding oxides due to a lower number of lone-pair electrons and a reduced number of hydrogen bonds with water molecules.

3) Mechanical properties of the ceramic thin films can be controlled by the energy ε_{bi}, delivered by the ion bombardment to the film during its growth. As shown on the example of ZrN thin films, if the ε_{bi} is sufficient enough, ceramic film exhibit high hardness (up to 23GPa) and enhanced resistance to cracking. Wetting properties of the ZrN films do not depend on the ε_{bi}.

4) Wetting properties of the low-electronegativity metals strongly depend on the thickness of the film. For HfO_2 films measurements show $\theta = 100°$ for the 2300nm thick film and $\theta = 120°$ for the 50nm thick film. This effect can be explained by the influence of the non-dominant texture and/or non-monotonic size dependence of the particle surface energy.

5) Small addition of oxygen during the deposition can significantly improve mechanical properties of the growing ZrTi alloy films. ZrTi(O) films show a nanocrystalline structure, excellent resistance to cracking during the bending ($\varepsilon = 2\%$) and high indentation load test. Also, ZrTi(O) films show much higher strength-to-weight ratio than common Ti and Zr alloys and metallic glasses.

8. AUTHOR'S LIST OF PUBLICATIONS

Referred journal papers:

1) **Zenkin, S**., Kos, S., Musil, J. *Hydrophobicity of Thin Films of Compounds of Low-Electronegativity Metals*. Journal of the American Ceramic Society 97, 2014, 2713-2717;

2) Musil, J., **Zenkin S**., Kos, S., Cerstvy, R., Haviar, S. *Flexible hydrophobic ZrN nitride films*. Vacuum 131, 2016, 34-38;

3) **Zenkin, S**., Belosludtsev, A., Kos, S., Cerstvy, R., Haviar, S., Netrvalova, M. *Thickness dependent wetting properties and surface free energy of HfO_2 thin films*. Applied Physics Letters 108, 2016, 231602;

4) Musil J., **Zenkin S**., Cerstvy R., Haviar S., Ciperova Z., *Physical and mechanical properties of crystalline and nanocrystalline Zr-Ti alloy films prepared by DC magnetron sputtering*, submitted

Contributions at scientific conferences:

1) **Zenkin, S**., Kos, S., Musil, J. *Hydrophobic and mechanical properties of transition-metal based ceramics*. Garmisch-Partenkirchen, Germany, 2014.

2) **Zenkin, S**., Kos, S., Musil, J. *Hydrophobicity of thin films of compounds of low-electronegativity metals*. Paris, France, 2015.

3) **Zenkin, S**., Belosludtsev, A., Kos, S., Cerstvy, R., Haviar, S., Netrvalova, M. *Thickness dependent wetting properties of thin films of ceramics based on low-electronegativity metals*. Prague, Czech Republic, 2016.

4) **Zenkin, S**., Belosludtsev, A., Kos, S., Cerstvy, R., Haviar, S., Netrvalova, M. *Thickness dependent wetting properties of thin films of ceramics based on low-electronegativity metals*. Lille, France, 2016.

5) **Zenkin, S**., Kos,S., Musil J., Belosludtsev, A., Cerstvy, R., Haviar, S., Netrvalova, M. *Low-electronegativity metal-based hydrophobic hard ceramics*. Pilsen, Czech republic

6) **Zenkin, S**., Belosludtsev, A., Kos, S., Cerstvy, R., Haviar, S., Netrvalova, M. *Thickness dependent wetting properties of thin films of ceramics based on low-electronegativity metals*. Garmisch-Partenkirchen, Germany, 2016.

ABSTRACT

Early transition metals and their oxides and nitrides are widely used in industrial applications due to their high hardness, thermal stability, transparency (in the case of oxides and some nitrides) and other unique combinations of properties. This PhD thesis is dedicated to the reactive magnetron sputtering of the multifunctional thin films based on transition metals. This thesis is divided onto 7 main chapters.

Chapter 1 is the general introduction discussing the magnetron sputtering and techniques used in the work for the films characterization. Chapter 2 shows the main aims of this PhD thesis. Chapters 3-6 show the main results of the PhD thesis in the form of journal articles.

Chapter 3 discusses about the role of electronegativity of the metal on the hydrophobicity and the surface free energy of its oxides and nitrides. It was shown that metals with low electronegativity $\chi = 1.1$-1.3 form hydrophobic oxide and nitride thin films. Also, the difference between the water droplet contact angle for oxides and nitrides was explained by the difference of their electronic structure and different number of the lone-pair electrons.

Chapter 4 shows the effect of the energy ε_{bi} delivered to ZrN thin films during their growth on their mechanical properties and resistance to cracking. ε_{bi} was controlled by the substrate bias during the deposition in the range from floating to -80V. We show that if ε_{bi} is sufficient enough, ZrN films exhibit very high hardness (up to 23GPa) and excellent resistance to cracking during the bending ($\varepsilon = 2\%$) and high indentation load test. Also, was shown that the value of ε_{bi} has no effect on the hydrophobicity of the ZrN films.

In Chapter 5 the influence of the film thickness on the hydrophobic properties of HfO_2 films was discussed. In the experiments the value of the water droplet contact angle was changed from 100° for the 2300nm thick film to 120° for the 50nm thick film. We suggest two possible explanations of this effect: influence of the non-dominant texture and/or non-monotonic size dependence of the particle surface energy. Also, the role of the surface contaminants in the hydrophobicity of HfO_2 films was discussed.

Chapter 6 discusses the deposition of crystalline and nanocrystalline thin films of the ZrTi alloy with different elemental composition. We show that a small addition of the oxygen during the deposition significantly decreases the crystallinity of ZrTi alloy. At the same time, hardness increases up to 16GPa (5GPa for ZrTi alloy without O_2 addition). Also, a small addition of O_2 enhances resistance to cracking of ZrTi alloy.

Chapter 7 contains the main conclusions of this PhD thesis.

RESUME ČESKY

Přechodové kovy a jejich oxidy a nitridy jsou široce používány v průmyslových aplikacích, díky vysoké tvrdosti, tepelné stabilitě, transparentnosti (v případě oxidů a některých nitridů) a dalším jedinečným vlastnostem. Tato disertační práce je zaměřena na reaktivní magnetronové naprašování multifunkčních tenkých vrstev na bázi přechodových kovů. Tato práce je rozdělena na 7 hlavních kapitol.

Kapitola 1 je obecný úvod ve kterém je diskutováno magnetronové naprašování a techniky používané pro charakterizaci filmů. Kapitola 2 ukazuje hlavní cíle této disertační práce. Kapitoly 3-6 ukazují hlavní výsledky disertační práce ve formě článků.

Kapitola 3 pojednává o roli elektronegativity kovu na hydrofobní vlastnosti a povrchové energie příslušných oxidů a nitridů. Bylo prokázáno, že kovy s nízkou elektronegativitou $\chi = 1{,}1\text{-}1{,}3$ vytváří hydrofobní oxidy a nitridy. Rozdíl kontaktního úhlu u oxidů a nitridů je vysvětlen pomocí jejich elektronové struktury a různého počtu neúplných elektronových párů.

Kapitola 4 ukazuje roli energie ε_{bi} dodané do tenkých vrstev ZrN v průběhu jejich růstu na jejich mechanické vlastnosti a odolnost proti praskání. ε_{bi} byla řízena předpětím na substrátu během naprašovaní v rozmezí od plovoucího potencialu do -80V. Je ukázáno, že je-li ε_{bi} dostatečně velká, vrstvy ZrN vykazují velmi vysokou tvrdost (až 23GPa) a vynikající odolnost proti vzniku trhlin při ohybu ($\varepsilon = 2\%$), a odolnost při vrypové zkoušce při velkém zatížení. Také, bylo prokázáno, že hodnota ε_{bi} nemá vliv na hydrofobnost vrstev ZrN.

V kapitole 5 byl diskutován vliv tloušťky vrstvy na hydrofobní vlastnosti vrstev HfO_2. V našich experimentech byl kontaktní úhel vodní kapky změněn z 100° pro vrstvu 2300nm na 120° pro 50 nm vrstvy. Dvě možná vysvětleníí tohoto efektu: Vliv nedominantní textury a / nebo nemonotónní závislosti velikosti povrchové energie částice. Také byla diskutována role povrchových nečistot v hydrofobnosti vrstev HfO_2.

Kapitola 6 pojednává o depozici krystalických a nanokrystalických tenkých vrstev slitiny ZrTi s různým elementárním složením. Ukázali jsme, že malé množství kyslíku v atmosféře během depozice výrazně snižuje krystalinitu slitin ZrTi. Současně se zvyšuje tvrdost až na 16GPa (5GPa pro slitiny ZrTi bez přidání O_2). Také maly přídavek O_2 zvyšuje odolnost k praskání ZrTi.

Kapitola 7 obsahuje hlavní závěry této disertační práce.